
Article:
Morgado, B.E. orcid.org/0000-0003-0088-1808, Sicardy, B. orcid.org/0000-0003-1995-0842, Braga-Ribas, F. orcid.org/0000-0003-2311-2438 et al. (56 more authors) (2023) A dense ring of the trans-Neptunian object Quaoar outside its Roche limit. Nature, 614 (7947). pp. 239-243. ISSN 0028-0836

https://doi.org/10.1038/s41586-022-05629-6

A dense ring of the trans-Neptunian object Quaoar outside its Roche Limit

B. E. Morgado[1,2,3], B. Sicardy[4], F. Braga-Ribas[5,2,3], J. L. Ortiz[6], H. Salo[7], F. Vachier[8], J. Desmars[9,8], C. L. Pereira[2,3], P. Santos-Sanz[6], R. Sfair[10,11], T. de Santana[4,11], M. Assafin[1,3], R. Vieira-Martins[2,1,3], A. R. Gomes-Júnior[12,11,3], G. Margoti[5], V. S. Dhillon[13,14], E. Fernández-Valenzuela[15], J. Broughton[16,17], J. Bradshaw[18], R. Langersek[19], G. Benedetti-Rossi[11,3], D. Souami[20,4,21], B. J. Holler[22], M. Kretlow[6,23,24], R. C. Boufleur[2,3], J. I. B. Camargo[2,3], R. Duffard[6], W. Beisker[23,24], N. Morales[6], J. Lecacheux[4], F. L. Rommel[2,3], D. Herald[17], W. Benz[25,26], E. Jehin[27], F. Jankowsky[28], T. R. Marsh[29], S. P. Littlefair[13], G. Bruno[30], I. Pagano[30], A. Brandeker[31], A. Collier-Cameron[32], H. G. Florén[31], N. Hara[33], G. Olofsson[31], T. G. Wilson[32], Z. Benkhaldoun[34], R. Busuttil[35], A. Burdanov[36], M. Ferrais[37], D. Gault[17], M. Gillon[38], W. Hanna[17], S. Kerr[17,39], U. Kolb[35], P. Nosworthy[17], D. Sebastian[40], C. Snodgrass[41], J. P. Teng[42], J. de Wit[36]

Planetary rings are observed not only around giant planets[1], but also around small bodies such as the Centaur Chariklo[2] and the dwarf planet Haumea[3]. Up to now, all known dense rings were located close enough to their parent bodies, being inside the Roche limit, where tidal forces prevent material with reasonable densities from aggregating into a satellite. Here we report observations of an inhomogeneous ring around the trans-Neptunian body (50000) Quaoar. This TNO has an estimated radius[4] of 555 km and possesses a ∼80-km satellite[5] (Weywot) that orbits at 24 Quaoar radii[6, 7]. The detected ring orbits at 7.4 radii from the central body, which is well outside Quaoar's classical Roche limit, thus implying that this limit does not always determine where ring material can survive. Our local collisional simulations show that elastic collisions, based on laboratory experiments[8], can maintain a ring far away from the body. Moreover, Quaoar's ring orbits close to the 1/3 Spin-Orbit Resonance[9] with Quaoar, a property shared by Chariklo's[2, 10, 11] and Haumea's[3] rings, suggesting that this resonance plays a key role in ring confinement for small bodies.

Within our efforts to characterize Quaoar's shape and search for putative material around it, we have predicted and observed several stellar occultations by this body. Following a report from Australia of a Neptune-like ring detected during a 2021 occultation and independently suspected in 2019, we have identified secondary events in previous occultations observed between 2018 and 2020 (Fig. 1, details in Extended Data Table. 1 and Supplementary Table 1, and Supplementary Fig. 1). They are consistent with a circular ring centered on the body, with two possible mirror solutions for the ring orientation, see Methods and Fig. 2. Both solutions have radii close to 4,100 km, or ∼7.4 Quaoar radii. One solution has a ring pole that presents a large mismatch with Weywot's orbital pole[7], while the other solution is consistent with a ring coplanar with Weywot's orbit (details in Table 1). This is our preferred solution, as a primordial collisional system surrounding Quaoar is expected to settle in a disk that subsequently forms both the ring and Weywot.

Each secondary event provides the radial width W_r, a mean normal opacity p and a mean normal optical depth τ of the ring, once projected in the ring plane[10, 11]. These quantities also provide the equivalent width ($E_p = pW_r$) and equivalent depth ($A_\tau = \tau W_r$) of each profile, see Methods and Table 1. A noteworthy result is the large variation of W_r and τ observed among

detections.

The 2019 June 5 occultation provided the ring profiles in four bands and our data do not show any significant dependence of E_p and A_τ with wavelength. This can be paralleled with multi-wavelength occultations by the core of Saturn's F ring, implying that this core contains a substantial population of particles larger than around 10 μm (refs.[12,13,14]). Moreover, our numerical integrations show that isolated particles smaller than 100 μm should escape the ring over a few years' time scale due to radiation pressure, see Methods.

Contrary to Chariklo's ring[11], Quaoar's ring is strongly irregular in azimuth. As such, it is reminiscent of Saturn's F ring that contains azimuthal features (clumps) or even local opaque structures interpreted as km-sized moonlets[15]. This clumpy nature is thought to be caused by the presence of thousands of small parent bodies (1- to 0.1-km in size) that collide and produce dense strands of micrometer- to centimeter-sized particles that re-accrete over a few months onto the parent bodies in a steady state regime[16,17,18]. A similar process may explain the patchy structure of Quaoar's ring. Another comparison can be made with respect to Neptune's Adams ring which also shows substantial longitudinal variations in optical depth.

In summary, our observations are consistent with a dense, irregular Quaoar's ring. The term 'dense' means that collisions play a key role in its dynamics. However, in contrast to all other known dense rings, Quaoar's ring orbits well outside the classical Roche limit. This excludes very tenuous dusty rings with $\tau < 10^{-4}$ seen for instance outside Saturn's Roche limit[19]. These tenuous rings are dominated by radiation effects that permanently remove them from their place of formation.

Objects orbiting at distance a from Quaoar with mass $M_{\rm Q}$ should have a density greater than the Roche critical density

$$\rho_{\rm Roche} = \frac{3M_{\rm Q}}{\gamma a^3} \qquad (1)$$

in order to avoid being disrupted by tidal forces. An often quoted value of γ is 1.6 which would correspond to a lemon-shaped particle aggregate filling its Roche lobe[20]. Using equation (1) and the values listed in Table 1, we obtain $\rho_{\rm Roche} \sim 30$ kg m^{-3}, corresponding to extremely porous or even fluffy material.

The dense rings of the giant planets[1], as well as Chariklo[2] and Haumea[3] lie within the Roche limit of the central bodies, assuming ρ=400 kg m^{-3}, typical of the small inner saturnian satellites[21]. With this value, Quaoar's classical Roche limit is near 1,780 km, much smaller than the ring radius of 4,100 km (Table 1 and Extended Data Fig. 2).

Numerical simulations of impact-generated disks show that material outside the Roche limit is expected to accrete over time scales of a few decades only[22,23]. This rapid processes would imply a very recent ring and, thus, a very low probability of being observed at the current epoch. That leaves us with a very young or extremely low density ring particles, or more likely, with the need for revisiting the Roche limit notion. In fact, equation (1) applies to a fluid satellite that is disrupted close to a planet. However, the reverse process – the accretion of colliding particles into a satellite – implies mechanisms not accounted for in equation (1).

Gravitational accretion of ring particles at a given distance depends not only on their bulk density ρ, but also on the radial velocity dispersion c between the particles. If $c \gg v_{\rm esc}$, where $v_{\rm esc}$ is the two-body escape velocity of the two ring particles involved in a pairwise impact, these impacts may avoid accretion outside the classical Roche limit One way to increase the radial

velocity dispersion is the ring material to be perturbed by external forces, such as resonances with Quaoar itself, Weywot, or undiscovered satellites. Another, is if collisions between pairs are sufficiently elastic so that their post-impact Hill-energies are positive[24]. In this scenario, the evolution of c is governed by a competition between collisional dissipation and viscous gain of energy from the orbital motion, leading to a steady-state velocity dispersion c_{st}. Its value depends on the relation $\epsilon(v_{\mathrm{n}})$ between the collisional coefficient of restitution ϵ and the perpendicular impact velocity between particles, v_{n}. In particular, steeper drops of ϵ vs. v_{n} result in smaller values of c_{st} (Fig. 3 and Extended Data Fig. 4).

Laboratory measurements show that for icy particles, ϵ depends sensitively on their surface properties. Figure 3 displays simulations of particle accretion in Quaoar's ring with τ=0.25, with $\epsilon(v_{\mathrm{n}})$ models covering the range of existing laboratory measurements. Initial measurements[25] with frost-covered ice at temperature T=210 K (referred to as Model 1) suggest that ϵ drops rapidly with v_{n}, attaining values below 0.5 for $v_{\mathrm{n}} \approx 1$ mm s^{-1}, relevant to Quaoar's ring (Fig. 3). In this case, c_{st} is of the order of v_{esc} and accretion sets in rapidly in the self-gravitating ring simulations as soon as ρ exceeds ρ_{Roche}, see Methods. In terms of the non-dimensional r_{H} parameter, defined in equation (8), this corresponds to $r_{\mathrm{H}} \approx$ 1.1-1.2, in agreement with simulations of accretion threshold in Saturn's rings[26].

However, better-controlled experiments[8] (referred to as Model 4) for particles with compacted-frost surfaces and lower temperatures 123 K indicated a much shallower $\epsilon(v_{\mathrm{n}})$ relationship. In this case the onset of accretion in Quaoar's ring requires ρ_{cr} larger than about 5,000 kg m^{-3}, corresponding to $r_{\mathrm{H}} > 5$. This leaves a safe margin to prevent accretion of icy ring particles with ρ=400 kg m^{-3}. The reason for this dramatically different behavior is the much higher c_{st} maintained by less dissipative impacts.

The accretion limits found above apply to optical depth $\tau \lesssim 0.25$. At larger τ the steady state value c_{st} decreases because the reduced mean free path between impacts leads to a less effective viscous gain (Extended Data Fig. 5, panel a). For example, for Model 4, the value of c_{st} decreases by a factor of nearly three as τ increases from 0.25 to 1, and the minimum value of ρ_{cr} required for accretion drops to about 300 kg m^{-3}. This is small, but still in line with the expected density of icy particles. Finally, the critical density ρ_{cr} also depends on the particle size R, ρ_{cr} increasing as R decreases, making a ring with smaller particles less prone to accretion, see Methods, (Extended Data Fig. 5 panel b). In summary, there are no objections for having a $\tau \lesssim 0.25$ non-accreting ring far outside Quaoar's classical Roche limit, provided that particles have compacted-frost surfaces described in ref.[8] (Model 4).

However, two problems remain concerning the presence of Quaoar's ring. One is that external perturbations may lead to local condensations. Enhancing τ reduces c_{st} and makes the ring prone to accretion. For example, Model 4 with ice particle densities of 400-900 kg m^{-3} would lead to this type of transition, as accretion is taking place for $\tau \gtrsim 1$ but not at smaller τ. The other problem is that impacts cause viscous spreading, which needs to be balanced by some mechanism to maintain the ring narrow, such as resonances.

Quaoar's ring is in fact close to both the outer Quaoar 1/3 Spin-Orbit Resonance (SOR) and the inner Weywot 6/1 Mean Motion Resonance (MMR), see Methods and Extended Data Fig. 2. As a small body, Quaoar is expected to have an irregular shape that creates significant SORs stemming from the non-axisymmetric terms of its potential[9]. A similar configuration is observed around Chariklo's and Haumea's rings (Methods), suggesting that the 1/3 SOR may play a key role in the ring confinement.

An assessment of the effect of the 1/3 SOR can be achieved through N-body collisional simulations with a ring that completely surrounds Quaoar. Such simulations applied to Chariklo actually show that the 1/3 SOR not only excites the orbital eccentricities of the particles as expected from equation (11), but also leads to a ring confinement near this resonance[27,28]. However, these simulations do not account yet for self-gravity. These results are encouraging but they require further simulations using more realistic parameters, as well as theoretical models to understand the confinement mechanism. If confirmed, the 1/3 SOR would play two roles. One is to confine the ring and the other one is to maintain a velocity dispersion between parent bodies or particle aggregates high enough to prevent further accretion.

The 6/1 Weywot MMR is a more complex resonance than the 1/3 Quaoar SOR because it involves one corotation-type resonance and five eccentricity-type resonances, see Methods. Their strengths and couplings depend on poorly constrained parameters, that is Weywot's mass, orbital eccentricity and apsidal precession rate. Our calculations show that the 6/1 corotation resonance creates one L_4-type Lagrange point that might concentrate Quaoar's ring material in a finite interval of longitudes if Weywot's orbital eccentricity e' is larger than about 0.1. At this stage of knowledge, neither of the two resonances is found to dominate the other. More observations are now necessary to pin down Quaoar's shape and Weywot's orbital elements, so that to better constrain the locations and strengths of the resonances that may interact with Quaoar's ring. Also, new detections of the dense region of the ring can be used to track its motion over time as another way to test models of resonant confinement.

Quaoar's ring is the third example of a dense ring around a small body found in the Solar System, suggesting that more still await discovery. Meanwhile, the large distance of this ring from Quaoar's means that the classical notion that dense rings survive only inside the Roche limit of a planetary body must be revised.

References

1. Esposito, L.W. & De Stefano M. in *Planetary ring systems* (eds Tiscareno, M. S. & Murray, C.D.) 2-29 (Cambridge Univ. Press, 2018).
2. Braga-Ribas, F. *et al.* A ring system detected around the Centaur (10199) Chariklo. *Nature* **508**, 72–75 (2014).
3. Ortiz, J.L. *et al.* The size, shape, density and ring of the dwarf planet Haumea from a stellar occultation. *Nature* **550**, 219–223 (2017).
4. Braga-Ribas, F. *et al.* The Size, Shape, Albedo, Density, and Atmospheric Limit of Transneptunian Object (50000) Quaoar from Multi-chord Stellar Occultations. *Astrophys. J.* **773**, 26 (2013)
5. Fornasier, S. *et al.* TNOs are Cool: A survey of the trans-Neptunian region. VIII. Combined Herschel PACS and SPIRE observations of nine bright targets at 70-500 μm. *Astron. Astrophys.* **555**, A15 (2015).
6. Fraser, W., Batygin, K., Brown, M. E. & Bouchez, A. The mass, orbit, and tidal evolution of the Quaoar-Weywot system. *Icarus* **222**, 357–363 (2013).
7. Vachier, F., Berthier, J. & Marchis, F. Determination of binary asteroid orbits with a genetic-based algorithm. *Astron. Astrophys.* **543**, A68 (2012).
8. Hatzes, A.P., Brigdes, F.G. & Lin, D.C.N. Collisional properties of ice spheres at low impact velocities. *Mon. Not. R. astr. Soc.* **231**, 1091–1115 (1988).

9. Sicardy, B., Leiva, R., Renner, S., Roques, F., El Moutamid, M. *et al.* Ring dynamics around non-axisymmetric bodies with application to Chariklo and Haumea. *Nature Astronomy* **3**, 146–153 (2019)

10. Bérard, D. *et al.* The Structure of Chariklo's Rings from Stellar Occultations. *Astron. J.* **154**, 144 (2017).

11. Morgado, B. *et al.* Refined physical parameters for Chariklo's body and rings from stellar occultations observed between 2013 and 2020. *Astron. Astrophys.* **652**, A141 (2021).

12. Bosh, A. S., Olkin, C. B., French, R. G. & Nicholson, P. D. Saturn's F Ring: kinematics and particle sizes from stellar occultation studies. *Icarus* **157**, 57–75 (2002).

13. Harbison, R. A., Nicholson, P. D. & Hedman, M. M. The smallest particles in Saturn's A and C Rings. *Icarus* **226**, 1225–1240 (2013).

14. Becker, T. M., Colwell, J. E., Esposito, L. W., Attree, N. O. & Murray, C. D. Cassini UVIS solar occultations by Saturn's F ring and the detection of collision-produced micron-sized dust. *Icarus* **306**, 171–199 (2018).

15. Murray, C.D. & French R.S. in *Planetary ring systems* (eds Tiscareno, M. S. & Murray, C.D.) 338-362 (Cambridge Univ. Press, 2018).

16. Cuzzi, J. N. & Burns J. A. Charged particle depletion surrounding Saturn's F ring: Evidence for a moonlet belt? *Icarus* **74**, 284–324 (1988).

17. Poulet, F., Sicardy, B., Nicholson, P.D., Karkoschka, E. & Caldwell, J. Saturn's Ring-Plane Crossings of August and November 1995: A Model for the New F-Ring Objects. *Icarus* **144**, 135–148 (2000).

18. Beurle, K., Murray, C. D., Williams, G. A., Evans, M. W., Cooper, N. J. & Agnor, C. B. Direct Evidence for Gravitational Instability and Moonlet Formation in Saturn's Rings. *The Astrophysical Journal Letters* **718**, L176–L180 (2010).

19. Hedman, M.M., Potsberg, F., Hamilton, D.P., Renner, S. & Hsu, H.-W. Dusty Rings. (eds Tiscareno, M. S. & Murray, C.D.) 308-337 (Cambridge Univ. Press, 2018).

20. Porco, C.C., Thomas, P.C., Weiss, J.W. & Richardson, D.C. Saturn's small inner satellites: clues to their origins. *Science* **318**, 1602 (2007).

21. Thomas, P. & Helfenstein, P. The small inner satellites of Saturn: Shapes, structures and some implications. *Icarus* **344**, 113355 (2020).

22. Kokubo, E., Ida, S. & Makino, J. Evolution of a circumterrestrial disk and formation of a single Moon *Icarus* **148**, 419–436 (2000)

23. Takeda, T. & Ida, S. Angular momentum transfer in a protolunar disk *Astrophys. J.* **560**, 514–533 (2001)

24. Ohtsuki, K. Capture probability of colliding planetesimals: dynamical constraints on accretion of planets, satellites, and ring particles. *Icarus* **106**, 228-246 (1993).

25. Bridges, F.G., Hatzes, A. & Lin, D.C.N. Structure, stability and evolution of Saturn's rings. *Nature* **309**, 333–333 (1984).

26. Karjalainen, R. & Salo, H. Gravitational accretion of particles in Saturn's rings. *Icarus* **172**, 328–348 (2004)

27. Salo, H. *et al.* Resonance confinement of collisional particle rings. *European Planetary Science Congress*, EPSC2021-338 (2021).

28. Sicardy, B. *et al.* Rings around small bodies: the 1/3 resonance is key. *European Planetary Science Congress*, EPSC2021-91 (2021).

29. Salo, H., Ohtsuki, K. & Lewis, M. C. Computer Simulations of Planetary Rings. in *Planetary ring systems* (eds Tiscareno, M. S. & Murray, C.D.) 434-493 (Cambridge Univ. Press, 2018).

30. Ortiz, J.L. *et al.* Rotational brightness variations in Trans-Neptunian Object 50000 Quaoar. *Astron. Astrophys.* **409**, L13–L16 (2013).

31. Morgado, B. E. *et al.* The stellar occultation by the trans-Neptunian object (50000) Quaoar observed by the ESA CHEOPS space telescope. *Astron. Astrophys.*, **664**, L15 (2022).

Acknowledgements
This work was carried out within the "Lucky Star" umbrella that agglomerates the efforts of the Paris, Granada and Rio teams, which is funded by the European Research Council under the European Community's H2020 (ERC Grant Agreement No. 669416). We thank C.D. Murray for help to calculate the expansion of Weywot's potential to sixth order in eccentricity. Part of the results were obtained using CHEOPS data. CHEOPS is an ESA mission in partnership with Switzerland with important contributions to the payload and the ground segment from Austria, Belgium, France, Germany, Hungary, Italy, Portugal, Spain, Sweden, and the United Kingdom. The CHEOPS Consortium would like to gratefully acknowledge the support received by all the agencies, offices, universities, and industries involved. Their flexibility and willingness to explore new approaches were essential to the success of this mission. The design and construction of HiPERCAM was funded by the European Research Council under the European Union's Seventh Framework Programme (FP/2007-2013) under ERC-2013-ADG Grant Agreement no. 340040 (HiPERCAM). HiPERCAM operations and VSD are funded by the Science and Technology Facilities Council (grant ST/V000853/1). The GTC is installed at the Spanish Observatorio del Roque de los Muchachos (ORM) of the Instituto de Astrofísica de Canarias (IAC), on the island of La Palma. This work has made use of data from the European Space Agency (ESA) mission Gaia (https://www.cosmos.esa.int/gaia), processed by the Gaia Data Processing and Analysis Consortium (DPAC, https://www.cosmos.esa.int/web/gaia/dpac/consortium). This study was financed in part by the National Institute of Science and Technology of the e-Universe project (INCT do e-Universo, CNPq grant 465376/2014-2). This study was financed in part by CAPES - Finance Code 001. The following authors acknowledge the respective i) CNPq grants: B.E.M. 150612/2020-6; F.B.R. 314772/2020-0; R.V.M. 307368/2021-1; M.A. 427700/2018-3, 310683/2017-3, 473002/2013-2. J.I.B.C. 308150/2016-3 and 305917/2019-6. ii) CAPES/Cofecub grant: B.E.M. 394/2016-05. iii) FAPERJ grants: M.A. E-26/111.488/2013. iv) FAPESP grants: A.R.G.Jr. 2018/11239-8; R.S. 2016/24561-0. v) CAPES-PrInt Program: G.B.R. 88887.310463/2018-00, Mobility number 88887.571156/2020-00. vi) DFG grants: R. S. 446102036. P.S-S. and R.D. acknowledge financial support by the Spanish grant AYA-RTI2018-098657-J-I00 "LEO-SBNAF" (MCIU/AEI/FEDER, UE). J.L.O., P.S-S., R.D. and N.M. acknowledge financial support from the State Agency for Research of the Spanish MCIU through the "Center of Excellence Severo Ochoa" award for the Instituto de Astrofísica de Andalucía (SEV-2017-0709), they also acknowledge the financial support by the Spanish grants AYA-2017-84637-R and PID2020-112789GB-I00, and the Proyectos de Excelencia de la Junta de Andalucía 2012-FQM1776 and PY20-01309. G.Br., I.Pa. acknowledge support from CHEOPS ASI-INAF agreement n. 2019-29-HH.0. A.B. was supported by the SNSA. A.C.C. and T.G.W. acknowledge support from STFC consolidated grant numbers ST/R000824/1 and ST/V000861/1, and UKSA grant ST/R003203/1. U.K. and R.B. acknowledge support by The OpenSTEM Labs, an

initiative funded by HEFCE and by the Wolfson Foundation J.d.W. and MIT gratefully acknowledge financial support from the Heising-Simons Foundation, Dr. and Mrs. Colin Masson and Dr. Peter A. Gilman for Artemis, the first telescope of the SPECULOOS network situated in Tenerife, Spain. The ULiege's contribution to SPECULOOS has received funding from the European Research Council under the European Union's Seventh Framework Programme (FP/2007-2013) (grant Agreement n° 336480/SPECULOOS), from the Balzan Prize and Francqui Foundations, from the Belgian Scientific Research Foundation (F.R.S.-FNRS; grant n° T.0109.20), from the University of Liege, and from the ARC grant for Concerted Research Actions financed by the Wallonia-Brussels Federation. TRAPPIST is a project funded by the Belgian Fonds (National) de la Recherche Scientique (F.R.S.-FNRS) under grant PDR T.0120.21. TRAPPIST-North is a project funded by the University of Liege, in collaboration with the Cadi Ayyad University of Marrakech (Morocco). E.J. is FNRS Senior Research Associate.

Author contributions

- B.E.M., B.S. and H.S. wrote the paper and made the figures, with major contributions from F.B.R, C.L.P., T.S., R.S., and F.V.
- F.B.R., B.S., J.D., J.L.O and P.S.S. organized the stellar occultation observational campaigns with the collaboration of W.Bei., and J.L.
- B.E.M., F.B.R., C.L.P., M.A., and G.M. analyzed the data and obtained the physical parameters presented in the paper, with inputs from B.S., J.L.O., P.S.S, and R.V.M.
- H.S designed and performed the N-body simulations and B.S., T.S., and R.S. performed dynamical studies presented in this project.
- F.V. computed Weywot orbital solution used in this project.
- B.E.M., A.R.G.J., R.C.B., G.B.R., F.L.R., and M.A. are the main developers of data analysis software utilized in this project.
- R.V.M., E.F.V., G.B.R., B.J.H., M.K., J.I.B.C., R.D., and D.So. collaborated with the interpretations of the results.
- F.J. and J.P.T observed Quaoar occultation in 02 September 2018.
- F.B.R., J.L.O, P.S.S., V.S.D., N.M., E.J., T.R.M., S.P.L., Z.B., R.B., A.Bu., M.F., M.G., U.K., D.Se., C.S., and J.W., participated in the observation of Quaoar occultation in 05 June 2019.
- W.Ben., G.B., I.P., A.Br., A.C.C., H.G.F., N.H., G.O., T.G.W. are members of ESA CHEOPS mission that detected Quaoar occultation in 11 June 2020, and the data analysis was done with major contributions from A.R.G.J.
- J.Bro., D.H. J.Bra., R.L., D.G., W.H., S.K., and P.N. observed Quaoar occultation in 27 August 2021, where J.Bro., R.L., and J.Bra. detected the dense arc of material within Quaoar ring.
- The opportunity to review the results and comment on the manuscript were given to all authors.

[1]Universidade Federal do Rio de Janeiro - Observatório do Valongo, Ladeira Pedro Antônio 43, CEP 20.080-090 Rio de Janeiro - RJ, Brazil
[2]Observatório Nacional/MCTI, R. General José Cristino 77, CEP 20921-400 Rio de Janeiro - RJ, Brazil
[3]Laboratório Interinstitucional de e-Astronomia - LIneA, Rua Gal. José Cristino 77, Rio de Janeiro, RJ 20921-400, Brazil
[4]LESIA, Observatoire de Paris, Université PSL, CNRS, UPMC, Sorbonne Université, Univ. Paris Diderot, Sorbonne Paris Cité, 5 place Jules Janssen, 92195 Meudon, France
[5]Federal University of Technology - Paraná (UTFPR / DAFIS), Rua Sete de Setembro, 3165, CEP 80230-901, Curitiba, PR, Brazil
[6]Instituto de Astrofísica de Andalucía, IAA-CSIC, Glorieta de la Astronomía s/n, 18008 Granada, Spain
[7]Space Physics and Astronomy Research unit, University of Oulu, FI-90014 Oulu, Finland
[8]Institut de Mécanique Céleste et de Calcul des Éphémérides, IMCCE, Observatoire de Paris, PSL Research University, CNRS, Sorbonne Universités, UPMC Univ Paris 06, Univ. Lille, France
[9]Institut Polytechnique des Sciences Avancées IPSA, 63 boulevard de Brandebourg, 94200 Ivry-sur-Seine, France
[10]Institut für Astronomie und Astrophysik, Eberhard Karls Universität Tübingen, Auf der Morgenstelle 10, 72076 Tübingen, Germany
[11]UNESP - São Paulo State University, Grupo de Dinâmica Orbital e Planetologia, CEP 12516-410, Guaratinguetá, SP, Brazil
[12]Institute of Physics, Federal University of Uberlândia, Uberlândia-MG, Brazil
[13]Department of Physics and Astronomy, University of Sheffield, Sheffield S3 7RH, UK
[14]Instituto de Astrofísica de Canarias, E-38205 La Laguna, Tenerife, Spain
[15]Florida Space Institute, University of Central Florida, 12354 Research Parkway, Partnership 1, Orlando, FL, USA
[16]Reedy Creek Observatory, Gold Coast, Queensland, Australia
[17]Trans-Tasman Occultation Alliance (TTOA), Wellington, PO Box 3181, New Zealand
[18]Samford Valley Observatory (Q79), Queensland, Australia
[19]Algester Astronomical Observatory, Queensland, Australia.
[20]Observatoire de la Côte d'Azur, Laboratoire Lagrange UMR7293 CNRS, Nice, France
[21]naXys, University of Namur, 8 Rempart de la Vierge, Namur, B-5000, Belgium
[22]Space Telescope Science Institute, Baltimore, MD, USA
[23]International Occultation Timing Association / European Section, Am Brombeerhag 13, D-30459 Hannover, Germany
[24]Internationale Amateursternwarte e.V. (IAS), Mittelstrasse 6, D-15749 Mittenwalde, Germany
[25]Physikalisches Institut, University of Bern, Sidlerstrasse 5, 3012 Bern, Switzerland
[26]Center for Space and Habitability, University of Bern, Gesellschaftsstrasse 6, 3012 Bern, Switzerland
[27]STAR Institute, Université de Liège, Allée du 6 août, 19C, 4000 Liège, Belgium
[28]Landessternwarte, Universität Heidelberg, Königstuhl, D-69117 Heidelberg, Germany
[29]Department of Physics, University of Warwick, Coventry CV4 7AL, UK
[30]INAF, Osservatorio Astrofisico di Catania, Via S. Sofia 78, 95123 Catania, Italy
[31]Department of Astronomy, Stockholm University, AlbaNova University Center, 10691 Stockholm, Sweden
[32]Centre for Exoplanet Science, SUPA School of Physics and Astronomy, University of St Andrews, North Haugh, St Andrews KY16 9SS, UK
[33]Observatoire Astronomique de l'Université de Genève, Chemin Pegasi 51, Versoix, Switzerland
[34]Oukaimeden Observatory, High Energy Physics and Astrophysics Laboratory, FSSM, Cadi Ayyad University, Marrakech, Morocco
[35]School of Physical Sciences, The Open University, Walton Hall, Milton Keynes MK7 6AA, UK

[36]Department of Earth, Atmospheric and Planetary Sciences, MIT, 77 Massachusetts Avenue, Cambridge MA 02139, USA
[37]Aix Marseille Univ, CNRS, CNES, Laboratoire d'Astrophysique de Marseille, Marseille, France
[38]Astrobiology Research Unit, Universit´e de Li'ege, All´ee du 6 Aoˆut 19C, B-4000 Li'ege, Belgium
[39]Astronomical Association of Queensland, 5 Curtis Street, Pimpama QLD 4209, Australia
[40]School of Physics & Astronomy, University of Birmingham, Edgbaston, Birmingham B15 2TT, United Kingdom
[41]Institute for Astronomy, University of Edinburgh, Royal Observatory, Edinburgh EH9 3HJ, UK
[42]AGORA Observatoire des Makes, AGORA, 18 Rue Georges Bizet, Observatoire des Makes, F-97421 La Rivière, France

Table 1 - Physical parameters of Quaoar, Weywot and the ring, with their 1-σ error bars.

Quaoar[a]			
Equivalent radius [km] (ref.[4])	Mass [$10^{21}\times$ kg]	Rotational Period [h] (ref.[30])	Radius of 1/3 Spin-Orbit Resonance[b] [km]
555.0 (2.5)	1.20 (0.05)	8.8494 (0.0002)	2,644 (37)
preferred rotation:		17.6788 (0.0004)	4,197 (58)
Weywot[a]			
Semi-major axis [km]	Eccentricity	Period [days]	Radius of 6/1 Mean Motion Resonance[a] [km]
13,289 (189)	0.056 (0.093)	12.4311 (0.0015)	4,021 (57)
Ring global parameters[c]			
Radius [km]	Pole RA [deg] (J2000)	Pole Dec [deg] (J2000)	Inclination relative to Weywot orbit[d] [deg]
Solution 1: 4,097.3 (9.5)	156.05 (0.89)	+81.40 (0.11)	43 (12)
Solution 2: 4,148.4 (7.4)	258.47 (0.87)	+54.14 (0.11)	6 (12)
Ring local parameters			
Date and Station[a]	Radial Width [km]	Normal optical depth	Equivalent Width [km]
02-09-2018 HESS (bef.)	22.29 (1.27)	0.016 (0.001)	0.62 (0.05)
05-06-2019 GTC g_s (bef.)	n.a[f]	n.a[f]	n.a[f]
05-06-2019 GTC r_s (bef.)	336.34 (23.81)	0.005 (0.002)	1.70 (0.41)
05-06-2019 GTC i_s (bef.)	301.38 (2.50)	0.004 (0.001)	1.04 (0.07)
05-06-2019 GTC z_s (bef.)	306.55 (2.36)	0.004 (0.001)	1.39 (0.10)
05-06-2019 GTC g_s (aft.)	109.68 (61.45)	0.009 (0.003)	0.87 (0.55)
05-06-2019 GTC r_s (aft.)	40.69 (4.83)	0.009 (0.001)	0.35 (0.04)
05-06-2019 GTC i_s (aft.)	44.09 (1.05)	0.008 (0.001)	0.35 (0.02)
05-06-2019 GTC z_s (aft.)	109.78 (63.00)	0.007 (0.002)	0.75 (0.45)
11-06-2020 CHEOPS (bef.)	n.a[g]	n.a[g]	1.03 (0.37)
11-06-2020 CHEOPS (aft.)	n.a[g]	n.a[g]	0.74 (0.38)
11-06-2020 Mount Carbine (aft.)	21.34 (3.13)	0.026 (0.008)	0.95 (0.26)
27-08-2021 Reedy Creek[h] (bef.)	$4.91^{+6.94}_{-0.43}$	$0.774^{+0.634}_{-0.645}$	$1.53^{+0.28}_{-0.81}$
27-08-2021 Algester[h] (bef.)	$6.69^{+2.56}_{-1.02}$	$0.504^{+1.107}_{-0.396}$	$1.78^{+0.73}_{-0.99}$
27-08-2021 Samford Valley[h] (bef.)	$7.09^{+0.86}_{-0.52}$	$0.118^{+0.021}_{-0.023}$	$0.71^{+0.10}_{-0.10}$

[a] The physical and orbital parameters of Quaoar and Weywot are obtained from the method described in ref.[7]. Details in Methods.

[b] From Kepler's third law $a = (GM_Q/n^2)^{1/3}$, assuming a spherical Quaoar of mass M_Q, where G is the gravitational constant and n is the mean motion.

[c] For each ring's pole orientation, an opposite direction is possible depending on the particles' direction of motion. Here, solution 2 is preferred, because it is closer to Weywot's orbital pole orientation.

[d] The uncertainty of the inclination between Weywot orbital pole (RA = 266 $\pm$ 10 degrees and Dec. +50 $\pm$ 6 degrees) and the ring pole is mostly dominated by Weywot.

[e] In each station, "(bef.)" stands for before the closest approach and "(aft.)" for after it.

[f] The light curve S/N does not allowed the detection of the ring.

[g] These values are not available as the ring is unresolved, only the Equivalent Width (Radial Width $\times$ Normal opacity) can be computed.

[h] Due the small number of points within each detections, the 1-sigma uncertainty has a large asymmetry.

Figure legends

Figure 1 | **Example of Quaoar's rings detections.** The observed flux (black points) and the models (red lines) are plotted against the time relative to the observer closest approach. The blue shaded regions are enlarged in corresponding underlying panels. Panels a, b and c: the light curve observed by HiPERCAM (i_s band) on the 10.4m Gran Telescopio Canarias (GTC) with closest approach time at 03:00:31.858 UTC (05 June 2019). Panels d, e and f: the light curve observed in Algester by R. Langersek (citizen astronomer) with closest approach time as 10:59:00.442 UTC (27 August 2021). No definite detection is made after closest approach, only an upper limit is derived. More detections are displayed in Supplementary Fig. 1.

Figure 2 | **Sky-plane projection of all our Quaoar's ring detections.** The occulting chords (green dashed line) and the ring detections with their 1-sigma error bars (red lines) are plotted for the 02 September 2018, 05 June 2019, 11 June 2020 and 27 August 2021 events. The black ellipses are the two simultaneous best-fitting solutions (Table 1), which are indistinguishable at this scale. The J2000 celestial North and East directions are shown in the upper right corner of each panel. Please note, that one of the chords in the 11 June 2020 occultations was obtained with CHEOPS space telescope, details in ref[31].

Figure 3 | **Local simulations of rings outside the classical Quaoar's Roche limit.** Results of self-gravitating local simulations performed with Quaoar's mass and ring radius (Table 1) showing the steady-state velocity dispersion c_{st} versus the bulk density ρ of the ring particles with assumed radius of 1 m. We used four velocity-dependent $\epsilon(v_n)$ models for the coefficient of restitution in impacts, spanning the range of various laboratory experiments of collisions between icy particles. Model 1 stands for Frost-covered ice spheres at temperature $T = 210$ K, $\epsilon(v_n) = (v_n/v_c)^{-0.234}$, with $v_c = 0.0077$ cm s^{-1} (ref.[25]); Model 2 for Frost-covered ice at $T = 123$ K, $\epsilon(v_n) = 0.48{v_n}^{-0.20}$ (ref.[8]); Model 3 for as Model 1 but with $v_c = 0.077$ cm s^{-1}; and Model 4 for particles of radius $R = 20$ cm with compacted frost at $T = 123$ K, $\epsilon(v_n) = 0.90\exp(-0.22v_n) + 0.01{v_n}^{-0.6}$ (ref.[8]), here v_n is the normal component of impact velocity (in cm/s). Also shown are simulations performed with a constant $\epsilon = 0.5$. The results are displayed both in terms of ρ and the dimensionless Hill parameter r_H. All simulations have optical depth $\tau = 0.25$, and follow a co-moving ring region with a size of 160 m $\times$ 160 m. Open circles along the lines denote simulations which did not lead to particle aggregation. Filled symbols stand for simulations where particles accreted to gravity-bound aggregates. The boxes show a snapshot of the co-moving ring region with and without the accretion of the particles for Model 1 and Model 4. The shaded region sketches the region where accretion takes place ($r_H \gtrsim 1.2$, $c/v_{esc} < 1.65 + 0.16\ln(\rho/80 \text{ kg m}^{-3}) \sim 2$), while the dashed line indicates the escape velocity at the surface of 1-m particles for a given bulk density ρ.

Methods

1 Prediction and observations

The four stellar occultations presented here were predicted using the standard procedures of the ERC *Lucky Star* project (https://lesia.obspm.fr/lucky-star) and are publicly available. The stars positions were obtained using Gaia Early Data Release 3 form[32]. Quaoar's ephemerides were derived from the Numerical Integration of the Motion of an Asteroid (NIMA[33]) integrator, taking advantage of Quaoar's accurate positions derived from previous occultations. For Weywot's ephemeris, we use the GENOID algorithm (GENetic Orbit IDentification[7, 34]) to fit an orbital model on the ten known observations of Weywot between 2006 to 2011 from the Keck observatory[6] and from a stellar occultation by Weywot, observed on 04 August 2019. It is a genetics-based algorithm that relies on a meta-heuristic method to find the most appropriate (i.e. minimum χ^2) set of dynamic parameters. On these data, the best results are from a Keplerian model of Weywot's motion around Quaoar.

Extended Data Table 1 provides astrometric and photometric information on the occultations and Supplementary Table 1 lists the circumstances of the observations. Ground-based stations and one space-borne instrument (the ESA/CHEOPS space telescope[31]) were mobilized.

2 Data Analysis

The images of the occulted stars (plus the occulting object) were analyzed applying standard aperture photometry procedures[35], using nearby reference stars to correct for sky transparency fluctuations. Secondary events (i.e., not caused by Quaoar itself) were observed on 02 September 2018, 05 June 2019, 11 June 2020 and 27 August 2021, revealing the presence of semi-transparent ring around Quaoar.

Abrupt opaque edges models, including the effects of diffraction, finite band width, exposure time and the Gaia DR2 stellar diameter, were fitted to the star dis- and re-appearances behind Quaoar's main body using the procedures within the Stellar Occultation Reduction and Analysis (SORA) package[36]. For the ring events, an additional parameter is the apparent ring opacity p' that measures the fractional drop of stellar flux. This parameter is related to the apparent optical depth τ' by

$$\tau' = -\ln(1-p'), \tag{2}$$

where 'apparent' refers to the quantity measured in the sky plane (see ref[11] and references therein). Knowing the ring pole orientation, these values can be converted to their values normal to the ring plane, p and τ. For cases where the Airy scale (see details in ref[37]) is larger than the width of the ring as seen in the sky plane and assuming a monolayer ring, p is given by

$$p = |\sin(B)| \left(1 - \sqrt{1-p'}\right), \tag{3}$$

and assuming a polylayer ring, τ is given by[38]

$$\tau = |\sin(B)| \frac{\tau'}{2}, \tag{4}$$

where B is the ring opening angle, $B = 0°$ (resp. $B = 90°$) corresponding to an edge-on (resp. pole-on) viewing, while Quaoar's ring has currently $B \sim -20$ deg (Extended Data Table 2). The integrals of p and τ over the radial width W_r of the rings define the equivalent width $E_p = pW_r$ and the equivalent depth $A_\tau = \tau W_r$ of the profile. The values of E_p and A_τ is proportional to the amount of material present in the profiles in the monolayer and polylayer case, respectively[10].

If the ring profile is not resolved (i.e. drop in flux occurs over less than three data points), p' is not known. However, the integral E_p is still measurable[10]. This is the case of the CHEOPS detections that has only one or two data points within the flux drops (Supplementary Fig. 1).

A noteworthy observational result is the large variation of W_r and τ observed among detections. For instance, the 2021 August 27 occultation shows a narrow and dense ring with $W_r \approx 8$ km and $\tau \approx 0.5$. This feature was detected from three different sites, covering about 5.1 degrees along the ring, corresponding to a local and dense ring-arc feature of at least 365 km in length. Conversely, the 2019 June 5 event reveals a wider and more transparent feature ($W_r \approx 300$ km, and $\tau \approx 0.014$). Meanwhile, the equivalent widths and equivalent depths vary in narrower ranges of about 0.3-1.7 km and 0.3-3.8 km, respectively (Table 1 and Extended Data Table 2).

Finally, the timings for the secondary events obtained at the various stations provide their sky-plane positions, to which an elliptical model is fitted using the χ^2-statistical test, with

$$\chi^2 = \sum_{i=1}^{N} \frac{(r_i - r'_i)^2}{\sigma_i^2 + \sigma_{\text{model}}^2}, \tag{5}$$

where r_i is the observed distance of the i^{th} data point to the ring center, r'_i is the corresponding distance of the model (the ellipse) and σ_i is the uncertainty on the distance associated with the timing uncertainty of the i^{th} data point. Finally, the σ_{model} parameter accounts for extra uncertainties associated with our model[11,36], stemming in particular from the unknown shape of Quaoar itself, resulting in model bias on its center position. Considering we have a single chord event that we fit an area equivalent circle of radius 555 km, but Quaoar's shape may be a Maclaurin spheroid[4] with an equatorial radius of 569 km and an oblateness of 0.087, this would cause a bias in the central position typically of ∼27 km, the value we choose for the σ_{model}.

Here, we assume that Quaoar's ring is circular, so that its apparent flattening f' projected in the sky plane is related to its opening angle B through

$$f' = 1 - \sin(B). \tag{6}$$

Assuming that Quaoar's ring pole orientation has been fixed over the 2018-2021 time interval, we used equation (5) to test a range of pole orientations and ring radii. This provides the two mirror solutions given in Table 1. Both solutions yield a satisfactory fit to the data, with best-fit χ^2 value per degree of freedom of $\chi^2_{\text{pdf}} = 0.28$ and $\chi^2_{\text{pdf}} = 1.02$, respectively. Solution 2 corresponds to a ring pole orientation that is consistent with Weywot's orbital pole orientation to within 6 ± 8 degrees, while Solution 1 results in a difference of 43 ± 8 degrees. Because we expect the ring and satellite to be coplanar, Solution 2 is our preferred one.

In summary, Quaoar's ring has a normal optical depth τ ranging from 0.004 to 0.77 depending on the longitude (Extended Data Tables 2 and 3). Using an impact frequency of $\sim 20\tau$ impacts per particle and per orbit[39], this implies that Quaoar's ring particles suffer between 1 and 10 collisions per revolution, which qualifies this ring as a dense one, that is a dynamics dominated by collisions. As the viewing geometry of the ring has changed very little between 2018 and

2021, and due to the paucity of observations, it is not possible yet to discriminate between a monolayer or a polylayer ring.

As a first approximation, we can parallel Quaoar ring with Saturn's rings, in that case, $\tau \sim 0.25$ corresponds to typical surface densities of $\Sigma \sim 500$ kg m^{-3} (ref.[40]). Adopting a radial width of $W_r = 8$ km for the densest part of the ring, and considering that the equivalent width of the ring remains roughly constant in longitude (Extended Data Table 2) – so that its mass per unit length is also roughly constant – we obtain a ring mass estimation of $M_r = 2\pi a\Sigma \sim 10^{14}$ kg, where $a \sim 4,100$ km is the ring radius. If accreted into a single satellite with bulk density of 400 kg m^{-3}, typical of the small inner saturnian satellites[21], this would yield body with a radius of the order of 5 km.

3 Multi-band profiles of the ring from GTC.

The 2019 June 05 event was monitored at the 10.4-meters *Gran Telescopio Canarias* (GTC) with the HiPERCAM instrument, using a four band system with g_s (0.40-0.55 μm), r_s (0.55-0.69 μm), i_s (0.69-0.82 μm), and z_s (0.82-1.00 μm) filters[41]. HiPERCAM also recorded the event in the u_s-band (0.3-0.4 μm), but the occulted star could not be detected at these wavelengths. Extended Data Fig. 1 displays the light curves obtained in each band, normalised between the unocculted and the zero stellar fluxes, respectively.

As expected, the noise decreases as the wavelength increases because the occulted star is brighter in the red. We fitted the ring parameters for each filter individually, see Table 1 and Extended Data Table 2. Even though we are fitting a ring detection with uniform opacity, we note that substructures may exist in some GTC profiles and thus may affect the obtained parameters, although any difference should be within the uncertainty of the parameters. No significant differences between the bands are observed in the parameters at the 3σ confidence level. Also, χ^2-tests were performed to compare pairs of observations around the ring detections. The largest difference showed a p-value of 0.021, meaning that there is a small 2.1% chance that the light curve obtained with the r_s (or z_s) filter is different from the g_s filter. All the remaining possibilities had a p-value smaller than 0.2%.

The absence of wavelength dependence indicates that Quaoar's ring contains a substantial population of particles larger than around 10 μm[12,13,14], which is in line with the dense and narrow rings of Saturn, Uranus and Chariklo.

4 Search for material in other light curves.

No light curves besides those described above show significant drops at the times expected from the ring geometry. This essentially stems from the lack of photometric sensitivity and/or temporal resolution of these data. We derived the detection limits provided by these data sets by calculating the standard deviation of the equivalent width

$$E_p(i) = \frac{|\sin(B)|}{2}[1 - \phi(i)]\Delta r(i), \tag{7}$$

where $\phi(i)$ is the observed flux and $\Delta r(i)$ is the radial interval covered by each exposure in the ring plane[37].

The limits of detection were evaluated using the data at their original spatial resolutions, and also after a resampling over 300-km windows, which corresponds to the widest ring profile in this project. When applied, resampling allows for increased sensitivity to small variations caused by large, diffuse structures. This procedure consists of applying a Savitsk-Golay digital filter on curves of equivalent width as a function of radial distance in the plane of the ring.

For example, W. Hanna's data set (27 August 2021) from Yazz had a closest distance approach to Quaoar's center of 1,690 km counted in the ring plane and covered a region about 20,000 km before the event, up to 16,000 km after it. No detection of secondary events were found up to a 3σ level of E_p=166 m per data point, with either an opaque ring (p=1) with radial width of $\sim$165 m, or a semi-transparent ring with W_r =2.7 km and p =0.06, or any other intermediate solutions. However, a wider and more transparent ($p \leqslant 0.01$) feature similar to what was observed with the GTC would be lost in the noise. All the obtained upper limits values can be found in Extended Data Table 3.

Besides the four events used here, we also revisited ten other Quaoar occultations observed since 2011 (ref.[42]) to search for secondary events. None of them provided data with sufficient quality to detect the ring.

5 N-body simulations of accretion.

We use numerical simulations with the local method where a co-moving ring patch of size 160×160 particle radii with periodic boundary conditions is followed to assess the accretion of particles for the proposed Quaoar ring. The particle impacts are calculated with a soft-particle method[43]. The number particles is N=2,000 in simulations with $\tau = 0.25$ and N=8,000 when $\tau = 1$; here τ stands for the dynamical optical depth defined as the total cross section of particles divided by the area of the simulated region. Such values of N are sufficient, since we are only interested in the onset of accretion, not the subsequent growth or mutual evolution of the aggregates, The advantage of a small N is that we can use a direct particle-particle method for calculation of self-gravity, to ensure that short-range binary interactions are accurately modeled. Typically, simulations lasted for 50-500 orbital periods (corresponding to time scales of a few years).

Several simulations were performed, varying the bulk density of particles ρ, and for a range of elasticity models (see below). We used Quaoar's mass M_Q and ring radius a given in Table 1. Identical particles with a radius R=1 m were assumed in most of our runs. The dimensionless r_H parameter characterizes the strength of self-gravity against the tidal force of the planet. It is defined as the ratio of the mutual Hill-radius (R_{Hill}) of a pair of particles to the sum of their physical radii,

$$r_H(\mu) = \frac{R_{Hill}}{R_1 + R_2} \tag{8}$$

where $\mu = M_1/M_2 = (R_1/R_2)^3$ is the mass ratio of the particles and

$$R_{Hill} = \left(\frac{M_1 + M_2}{3M_Q} \right)^{1/3} a.$$

If we consider a test particle at rest on the surface of a synchronously rotating spherical large particle (i.e., $\mu = 0$), the case $r_H(0) = 1$ corresponds to the limiting case of a zero net attraction

(tidal + self-gravity + centrifugal). Thus, in general, accretion (resp. disruption) of the pair is expected for r_H larger (resp. smaller) than unity. In the case of equal-mass particles ($\mu = 1$), we have

$$r_H = 2.62 \left(\frac{M_Q}{1.2 \times 10^{21} \text{ kg}} \right)^{-1/3} \left(\frac{\rho}{900 \text{ kg m}^{-3}} \right)^{1/3} \left(\frac{a}{4,100 \text{ km}} \right),$$

where $r_H(1)$ is denoted by r_H for simplicity. In the initial state of the simulation the radial velocity dispersion c exceeds by a large factor its steady-state value and also the 2-body escape velocity,

$$v_{esc} = \sqrt{2GM/R} \approx 0.07 \left(\frac{\rho}{900 \text{ kg m}^{-3}} \right)^{1/2} \left(\frac{R}{1 \text{ m}} \right) \text{ cm s}^{-1}. \quad (9)$$

During the simulation, c gradually decreases from its initial value due to collisional dissipation, until a steady-state value c_{st} is reached, when the dissipation and viscous gain balance each other, or until c drops to about $2v_{esc}$, in which case the particles start to accrete and rapidly coalesce into a single aggregate, see Extended Data Fig. 3. This transition from non-accreting to accreting behavior is very sharp when ρ is increased. In case of accretion, we record the value of c at the onset of aggregate growth, in practice at the instant when the impact frequency had sharply increased 2-fold compared to its average value. Usually, the aggregate becomes visually evident within one orbital period from this instant of time.

Elasticity models. Extended Data Fig. 4 illustrates the $\epsilon(v_n)$ models used in our simulations. It also shows the theoretical relation between optical depth τ and the critical ϵ_{cr} required for a balance between dissipation and viscous gain of energy[44]. The c_{st} depends on the $\epsilon(v_n)$ model via the $\epsilon_{cr}(\tau)$ relation and is independent of R as long as systems with $c_{st} \gg Rn$ are considered.

The specific values used in simulations, $\tau = 0.25$ and $\tau = 1.0$, are highlighted and the corresponding values of $\epsilon_{cr}(\tau)$ are marked on the left-hand plot. The small downward arrows for Model 4 illustrate the expected drop in the average steady-state v_n (proportional to c_{st}) when optical depth increases: basically this drop follows from less effective viscous gain at large τ due the reduction of mean free path between impacts. Similarly, for a fixed τ, the Models 3, 2 and 1 imply successively smaller average v_n's and c_{st} (refs.[45, 29]).

Accretion in simulations. The classical Roche limit applies for tidal disruption of a fluid satellite when brought gradually closer to the central body. It can be written in the form of Roche critical density for a given distance (equation (1)), where $\gamma = 0.849$ as in the original analysis by Roche[46]. However, besides a and ρ, the accretion of ring particles also depends on c, and thereby on the elasticity of particles.

Previous local N-body simulations[26] explored the onset of particle accretion in Saturn's rings, using both constant ϵ and the $\epsilon(v_n)$ relationship of Model 1 (ref.[25]). The dependence on distance and bulk density was parameterised with the r_H parameter (equation (8)). These simulations showed that $r_H > 1.1-1.2$ leads to accretion: the upper value is for identical frictionless particles like in the current experiments, whereas the lower value includes simulations with friction and/or particle size distribution. Note that the above condition for accretion is more stringent than the tidal destruction limit $\gamma = 1.6$ usually adopted (ref.[20]), which corresponds to $r_H > 0.87$. However, it is quite close to the classical value $\gamma = 0.849$ which corresponds to $r_H > 1.07$.

All simulations of ref.[26] were limited to elasticity models (constant $\epsilon \leq 0.5$ or the relationship $\epsilon(v_n)$ of Model 1) which correspond to fairly inelastic particles. In this case, the balance between dissipation and viscous gain leads to small velocity dispersion for all ring optical depths. In particular, the velocity dispersion maintained by impacts alone is between $\sim 2Rn$ and $\sim 3Rn$

(where n is the mean motion) and is of the same order as the 2-body escape velocity.

However, these highly dissipative models were compared in ref[29] to impact models with more elastic particles, and corresponding to our Model 4 (based on Fig. 22 of ref.[8]). In this case, no accretion was possible even with $r_{\mathsf{H}} = 1.23$, which was the largest value explored. This stems from the high velocity dispersion which now exceeds the 2-body escape velocity by a large margin.

The simulations presented here extend these studies to larger r_{H}. The behavior in N-body simulations is also consistent with 3-body integrations[24] which indicate that the probability of sticking in binary impacts increases rapidly when $r_{\mathsf{H}} \gtrsim 1.2$. The 3-body integrations (see Fig. 14.18 of ref.[45]) also indicate that for large r_{H}, the accretion probability goes rapidly down when impact velocities exceed 2-body escape velocity, in agreement with our current N-body experiments.

6 The dynamical environment of Quaoar's ring.

Table 1 lists the orbital radii of the 1/3 spin-orbit resonance (SOR) with Quaoar and the 6/1 mean motion resonance (MMR) with Weywot, assuming Keplerian motion around a spherical Quaoar of mass M_{Q}. The error bars on the resonance locations are dominated by the uncertainty on M_{Q}. Accounting for a possible large oblateness of Quaoar would shift these locations by a few kilometers only, leaving our conclusions unchanged. Moreover, Quaoar's rotational light curves yield two possible rotation periods[30]. The short rotation period (8.8394 ± 0.0002 h) would correspond to a single-peaked lightcurve, which would be caused by an oblate body with albedo features on its surface. However, we know that Quaoar cannot be an oblate spheroid but a triaxial ellipsoid due to the varying projected shape of the main body that we have determined in several stellar occultations by Quaoar (whose analysis is beyond the scope of this paper). Because triaxial ellipsoids give rise to double peaked lightcurves, the preferred rotation period is 17.6788 ± 0.0004 h. Besides, this double-peaked solution provided a better fit to the photometric data [30].

The first-order (in the particle orbital eccentricity) SOR resonances – also called Lindblad resonances – exert torques that clear over short time scales (a few Myr) the region straddling the corotation region near 2,020 km, where the orbital period of the particles matches the rotation period of the body[9]. This clearing proceeds up to the outermost 1/2 Lindblad resonance near 3,200 km. Moving outwards the next resonance is the second-order 1/3 SOR, that occurs at a semi-major axis of $a_{1/3} = 4,197 \pm 58$ km. This matches within the error bars with the two possible solutions for the ring orbital radius $a_{\mathsf{R1}} = 4,097.3 \pm 9.5$ km and $a_{\mathsf{R2}} = 4,148.4 \pm 7.4$ km, at the 1.7 and 0.9σ levels, respectively. Similarly, the 6/1 Weywot mean motion resonance is at $a_{6/1} = 4,021 \pm 57$ km, again matching the two solutions a_{R1} and a_{R2}, at the 1.2 and 2.1σ levels, respectively.

We note that the two ring systems discovered around Chariklo and Haumea orbit also near the 1/3 SOR with their central bodies. For Chariklo, $a_{1/3} = 408 \pm 20$ km (ref.[47]), while its two rings orbit at 386 km and 400 km from the body[11]. Similarly, for Haumea we have $a_{1/3} = 2,285 \pm 8$ km, while the ring orbits at $2,287^{+75}_{-45}$ km (ref.[3]).

Using equation (1) and $\rho = 400$ kg m^{-3}, typical of the small inner saturnian satellites[21], we obtain a Quaoar's Roche limit near 1,780 km. Finally, the Quaoar corotation (or synchronous) orbit is at $2,018 \pm 28$ km. Extended Data Fig. 2 summarizes the various radii of interest

mentioned here.

We now consider resonances between a massless ring particle and either a Quaoar's mass anomaly or Weywot. For simplicity, Quaoar's mass anomaly is described as a hemispheric mountain at the surface of the body, see main text, however, it may also be an internal feature within an otherwise oblate, smooth body. We denote a, e, λ, ϖ, n and $\kappa = n - \dot{\varpi}'$ the semi-major axis, orbital eccentricity, mean longitude, longitude of pericenter, mean motion and epicyclic frequency of the particle, respectively. Depending on the case, λ' is the orientation of Quaoar's mass anomaly or Weywot's mean longitude, while n' is either Quaoar's spin rate or Weywot's mean motion. In the case of Weywot, the orbital eccentricity and the longitude of pericenter of the satellite, e' and ϖ', must also be accounted for (contrarily to the mass anomaly, since the latter moves along a circle). Then $\kappa' = n' - \dot{\varpi}'$ is Weywot's epicyclic frequency. The quantities a_0 and n_0 are the radius and the mean motion at exact resonance. Finally, Quaoar's and Weywot's mass anomaly are denoted by μ_{Q} and μ_{W}, respectively, both normalized to Quaoar's mass.

We consider the resonance condition $n_0/n' = m/(m-j)$, where m is a positive or negative integer and j is positive. This resonance splits into $j+1$ resonances, each described by a Hamiltonian of the form

$$\mathcal{H}(X,Y;\Delta J) = -\frac{3}{2}n_0\left[\Delta J - \left(\frac{m-k}{2k}\right)\left(X^2+Y^2\right)\right]^2 + \epsilon_k n_0 e^k e'^{j-k}\cos(\psi_k), \tag{10}$$

where $\psi_k = m\lambda' - (m-j)\lambda - k\varpi - (j-k)\varpi'$, and where $k = 0, ...j$ is the order of the resonance in the particle's eccentricity. The case $k=0$ corresponds to a corotation-type resonance with critical angle $\phi_0 = \psi_0 = m\lambda' - (m-j)\lambda - j\varpi'$, while the cases $k \neq 0$ correspond to eccentricity-type resonances with critical angles $\phi_k = \psi_k/k$.

Each value of k is in fact associated with a mean motion resonance $n_0/n' = (m-j+k)/(m-j)$ of order k between the particle and a potential moving at the pattern speed

$$\Omega_k = n' + \frac{j-k}{m-j+k}\kappa'.$$

For $k \neq 0$, we define the eccentricity vector as $(X,Y) = [e\cos(\phi_k), e\cos(\phi_k)]$, where $e^2 = X^2+Y^2$. The Hamiltonian $\mathcal{H}$ is parameterized by the Jacobi constant

$$\Delta J = \frac{1}{2}\left(\frac{\Delta a}{a_0} + \frac{m-k}{k}e^2\right),$$

where $\Delta a = a - a_0$ is the distance to the resonance. Particles with the same value of ΔJ but different initial conditions for (X,Y) follow level curves of $\mathcal{H}$ under the Hamiltonian flow $\dot{X} = -\partial\mathcal{H}/\partial Y$ and $\dot{Y} = +\partial\mathcal{H}/\partial X$, eventually forming the phase portrait of the resonance.

The resonant forcing is encapsulated in the perturbing term containing ϵ_k in the right-hand side of equation (10), not to be confused with the coefficient of restitution ϵ used in the main text and in Section 5. It is proportional to μ_{Q} or μ_{W}, and its numerical values is derived from expansion of the disturbing potential of the mass anomaly[48] or the satellite[49].

7 The 1/3 Spin-Orbit Resonance (SOR).

The 1/3 SOR resonance corresponds to $m=-1$ and $j=2$ in equation (10), so that $n/\Omega = 1/3$, where the pattern speed Ω is Quaoar's spin rate. Because the mass anomaly moves on a circle,

only the resonance $k = j$ (=2 here) is allowed, so that

$$\mathcal{H}(X, Y; \Delta J) = -\frac{3}{2} n_0 \left[\Delta J + \frac{3}{4} \left(X^2 + Y^2 \right) \right]^2 + \epsilon_{1/3} n_0 \left(X^2 - Y^2 \right),$$

where the subscript 1/3 refers to the 1/3 SOR, and where we have omitted, for brevity, the index $k = 2$ that should appear for the coefficient ϵ. Similarly, the resonant angle is denoted $\phi_{1/3} = (-\lambda' + 3\lambda - 2\varpi)/2$, and $\Delta J = [\Delta a/a_{1/3} - (3/2)e^2]/2$. From the expression of $\mathcal{H}(X, Y; \Delta J)$, it results that for an interval of ΔJ of width $8|\epsilon_{1/3}|/9$ centered on the resonance, the origin $(X, Y) = (0, 0)$ of the phase portrait is a fixed hyperbolic (and thus unstable) point. Collisions tend to damp the eccentricities, i.e., force the particles to move towards the origin of the phase portrait (i.e., on circular orbits). Conversely, in the interval mentioned above, the resonance tends to force them to follow eight-shaped trajectories, and thus, to acquire non-zero eccentricities. From the expression of ΔJ, this happens for a interval of semi-major axes of width $W = (16|\epsilon_{1/3}|/9)a_{1/3}$ centered on the resonance value $a_{1/3}$.

The forced eccentricity then reaches a peak value (Extended Data Fig. 6) of

$$e_{\mathsf{peak},1/3} = \frac{8}{3}\sqrt{\frac{|\epsilon_{1/3}|}{3}} = 0.118\sqrt{\mu_{\mathsf{Q}}} = 0.0834 \left(\frac{h}{R_{\mathsf{Q}}} \right)^{3/2} \tag{11}$$

at $a = a_{1/3}[1 - (8/9)\epsilon_{1/3}]$, where we have used the expression of $\epsilon_{1/3}$ in Extended Data Table 4. In the second equation, we have assumed that the mass anomaly takes the form of a hemispheric mountain of height h at Quaoar's surface, see main text.

The peak eccentricity $e_{\mathsf{peak},1/3}$ tends to maintain a velocity dispersion Δv among the particles or putative parent bodies of Quaoar's ring (main text). If the motions of these bodies are not coherent, we have

$$\Delta v = 2 e_{\mathsf{peak},1/3} v_{\mathsf{orb}}, \tag{12}$$

where $v_{\mathsf{orb}} = \sqrt{GM_{\mathsf{Q}}/a_{1/3}}$ is the orbital velocity at the resonance. The escape velocity at the surface of a particle with radius R_{p} and density ρ is $v_{\mathsf{esc}} = \sqrt{8\pi G \rho R_{\mathsf{p}}/3}$. Consequently, the velocity dispersion Δv is comparable to v_{esc} for

$$\mu_{\mathsf{Q}} \sim 2 \times 10^{-4} R_{\mathsf{p,km}}^2, \tag{13}$$

where we have used equation (11), $\rho = 400$ kg m^{-3} and the numerical values of Table 1.

In the presence of collisions, the second-order nature of the 1/3 SOR leads to mathematical difficulties. In particular, the periodic resonant streamlines intersect at one point, even for vanishing eccentricities[48]. This yields to a multi-valued velocity field and infinite densities, and therefore singularities in the hydrodynamical equations.

Considering the simple case of a mass anomaly in the form of a hemispheric mountain of height h on Quaoar's surface, the mass anomaly normalized to Quaoar's mass is $\mu_{\mathsf{Q}} = (h/R_{\mathsf{Q}})^3/2$, where R_{Q} is Quaoar's radius. The 1/3 SOR resonance forces an eccentricity $e_{\mathsf{peak},1/3}$ (equation (11)) which can in turn maintain locally a velocity dispersion among the putative parent bodies in Quaoar's ring (equation (12)). This velocity dispersion is comparable to the escape velocity at the surface of the parent bodies for a certain value of μ_{Q} (equation (13)), or equivalently, for a certain mountain height of

$$h_{\mathsf{km}} \sim 40 R_{\mathsf{p,km}}^{2/3}. \tag{14}$$

Assuming parent bodies with size $R_{\mathsf{p}} \sim 0.1$ km, typical of Saturn's F ring parent bodies, we obtain $h \sim 10$ km. Thus, plausible topographic features on Quaoar are indeed able to maintain

a velocity dispersion among the parent bodies that prevent them from accreting near the 1/3 SOR. This is the case a fortiori for ring particle aggregates that have much smaller sizes. This assumes, however, that the resonant responses of the bodies are not coherent. In the opposite case, the velocity dispersion in equation (12) could be largely overestimated.

Meanwhile, more realistic numerical simulations using N-body collisional codes do show that confinement of a collisional disk (without self-gravity) is observed near the 1/3 SOR with Chariklo's[28,27]. This confinement is associated with angular momentum flux reversal at certain longitudes of the ring, but is not yet backed up by analytical calculations.

8 The Weywot 6/1 Mean-Motion Resonance (MMR).

The 6/1 MMR Weywot resonance corresponds to $m = 6$ and $j = 5$ in equation (10). It splits into six resonances as k takes the values 0,...5, with the respective resonant angles listed in Extended Data Table 4. The associated resonant terms of Weywot's disturbing potential have amplitudes of the form $\epsilon_{6/1,k} e^k e'^{5-k}$, where the coefficients $\epsilon_{6/1,k}$ are given in Extended Data Table 4.

Corotation resonance. The case $k = 0$ corresponds to the corotation resonance condition $n = n' + 5\kappa' \approx 6n'$. It creates one stable elliptic (L_4 or L_5-type) Lagrange point and one unstable hyperbolic (L_3-type) point. Here we consider the possibility that the accumulation of ring material around the L_4 point might explain the longitudinal variability of Quaoar's ring. Classical calculations provide the full width of the corotation zone:

$$W_{\rm COR} = \left(\frac{64}{3}\epsilon_{6/1,0}\right)^{1/2} a_0,$$

that corresponds to the spread in semi-major axes of the particles trapped in this corotation resonance. Using the value of $\epsilon_{6/1,0}$ (Extended Data Table 4), $a_0 \approx 4020$ km (Table 1), and assuming that Quaoar and Weywot have the same bulk density, we obtain

$$W_{\rm COR} \approx 7100 \left(\frac{R_{\rm W}}{R_{\rm Q}}\right)^{3/2} e'^{5/2} \text{ km},$$

where $R_{\rm W}$ is Weywot's radius. Both the quantities $R_{\rm W}$ and e' (Weywot's orbital eccentricity) are poorly constrained. Assuming the same albedo for Quaoar and Weywot, we obtain $R_{\rm W} \approx 40$ km (ref.[5]), and Weywot's orbital solution provides $e' < 0.15$ (using the method presented in ref.[34]). The equation above then yields $W_{\rm COR} \lesssim 1$ km.

This is comparable to the spread in semi-major axis of Neptune's arcs, which is much smaller than the physical width of Neptune's ring-like arcs, about 15 km. This is classically explained by the coherent radial motion of Neptune's arc particles forced by the nearby satellite Galatea[50]. This process might also apply to Quaoar's ring, but still remains to be established. Meanwhile, we note that $W_{\rm COR}$ rapidly decreases with e'. For instance, for $e' = 0.01$, we obtain $W_{\rm COR} \sim 1$ m, which appears to be too narrow for maintaining an arc structure around Quaoar, as $W_{\rm COR}$ is then comparable to the expected typical particle sizes.

Lindblad resonance. The resonance with $k = 1$ corresponds to a Lindblad (first-order) resonance with associated disturbing potential $\epsilon_{6/1,1} e e'^4 \cos(\phi_{6/1,1})$. Technically, it is a 2/1 resonance of the particle with the component of Weywot's potential that has the pattern speed

$n' + 2\kappa' \approx 3n'$. The same exercise as for the Quaoar 1/3 SOR, but now considering a first-order resonance, shows that this resonance forces a peak eccentricity for particles that start with a circular orbit of

$$e_{\mathrm{peak},6/1} = \left(\frac{32}{3}\epsilon_{6/1,1}e'^4\right)^{1/3} = 2.921\left(\frac{R_{\mathrm{W}}}{R_{\mathrm{Q}}}\right)e'^{4/3}. \quad (15)$$

The value of $e_{\mathrm{peak},6/1}$ is again poorly constrained. However, we may compare $e_{\mathrm{peak},6/1}$ and $e_{\mathrm{peak},1/3}$ (equation 11) for $R_{\mathrm{W}} = 40$ km and $h = 10$ km. Then the two values of e_{peak} are comparable for a Weywot's orbital eccentricity as small as 0.005. In other words, Weywot's is expected to force eccentricities of the ring at the 6/1 Lindblad resonance that are comparable to or larger than the eccentricities forced by Quaoar's 1/3 SOR.

Other resonances. The cases $k = 2, ...5$ correspond to four additional resonances of orders k in the particle eccentricities. At this stage, it is difficult to assess their interactions and effects on the corotation and Lindblad resonances, and thus, on the ring behavior. In particular, their mutual radial distances depend on the value of the apsidal precession rate $\dot{\varpi}'$, which is unknown. Moreover, their couplings also depend on the value of e', which is largely unconstrained.

9 The effect of radiation pressure.

Even though Quaoar is located in a faraway region compared to the giant planets, the weak gravity field of the central body allows micrometric ring particles to be strongly disturbed by the radiation pressure (RP). To first order, this force causes no secular effect in the semi-major axis of the particles, but induces periodic oscillations in the eccentricity. In a first approximation, the maximum eccentricity e_{RP} attained by a particle of radius R, bulk density ρ initially in a circular orbit of radius a is[51]

$$e_{\mathrm{RP}} = \frac{2C}{1+C^2}, \quad \text{with} \quad C = \frac{9}{8}\frac{n}{n_{\mathrm{Q}}}\frac{Q_{\mathrm{pr}}F_{\odot}a^2}{GM_{\mathrm{Q}}c'\rho R}, \quad (16)$$

where n and n_{Q} are the mean motion of the particle and Quaoar, respectively, c' is the speed of light, $F_{\odot}$ is the solar flux at Quaoar's orbit, and Q_{pr} is the radiation pressure coefficient, equal to unity for an ideal material.

This equation shows that ring particles smaller than about 25 μm in radius are ejected from the system, while grains with radius $\lesssim 45$ μm reach eccentricities large enough to collide with Quaoar. In fact, particles smaller than 0.2 cm suffer radial excursions that surpass the ring width.

These results are backed up by numerical simulations performed with a modified version of the Mercury package[52] that includes the radiation pressure effects. These simulations show that 1 μm-particles are ejected from the system in less than a couple of years, while $\lesssim 45$ μm do not survive over a few decades. These results show that Quaoar's ring is likely to be quickly depleted of sub-cm grains, in agreement with the GTC multi-filter observations.

References

32. Brown, A. G. A. *et al.* Gaia Early Data Release 3. *Astron. Astrophys.* **649**, A1 (2021).

33. Desmars, J. *et al.* Orbit determination of trans-Neptunian objects and Centaurs for the prediction of stellar occultations. *Astron. Astrophys.* **584**, A96 (2015).

34. Vachier, F., Carry, B. & Berthier, J. Dynamics of the binary asteroid (379) Huenna. *Icarus* **382**, 115013 (2022).

35. Assafin, M. *et al.* PRAIA - Platform for Reduction of Astronomical Images Automatically. *Gaia follow-up network for the solar system objects : Gaia FUN-SSO workshop proceedings*, p. 85-88 (2011).

36. Gomes-Júnior, A. R., Morgado, B. E. *et al.* SORA: Stellar occultation reduction and analysis. *Mon. Not. R. Astron. Soc.* **511**, 1167–1181 (2022).

37. Boissel, Y. *et al.* An exploration of Pluto's environment through stellar occultations. *Astron. Astrophys.* **561**, A144 (2014).

38. Elliot, J. L., French, R. G., Meech, K. J., & Elias, J. H. *The Astron. Journal*, **89**, 1587 (1984).

39. Hämeen-Anttila, K. A.& Salo, H. Generalized Theory of Impacts in Particulate Systems *Earth, Moon and Planets*, **62**, 1, 47-84 (1993).

40. Colwell, J. E., Nicholson, P. D., Tiscareno, M. S., *et al.* The structure of Saturn's rings. In: Dougherty, M. K., Esposito, L. W., and Krimigis, S. M., eds., Saturn from Cassini-Huygens, *Springer*, 375-412 (2009).

41. Dhillon, V. *et al.* HiPERCAM: a quintuple-beam, high-speed optical imager on the 10.4-m Gran Telescopio Canarias *Mon. Not. R. Astr. Soc.* **507**, 350–366 (2021).

42. Braga-Ribas, F. *et al.* Database on detected stellar occultations by small outer Solar System objects. *Journal of Physics: Conference Series* **1365**, 012024 (2019).

43. Salo, H. Simulations of dense planetary rings. III. Self-gravitating identical particles. *Icarus* **117**, 287–312 (1995)

44. Goldreich, P. & Tremaine, S. The velocity dispersion in Saturn's rings. *Icarus* **34**, 227–239 (1980).

45. Schmidt, J. *et al.* Dynamics of Saturn's dense rings. in Saturn from Cassini-Huygens (eds Dougherty, M.K., Esposito, L.W. & Krimigis S.M.) 413–458 (Springer, 2009).

46. Chandrasekhar, S. Ellipsoidal figures of equilibrium (Dover, 1987).

47. Leiva, R. *et al.* Size and Shape of Chariklo from Multi-epoch Stellar Occultations. *Astron. J.* **154**, 159 (2017).

48. Sicardy, B. Resonances in Nonaxisymmetric Gravitational Potentials. *Astron. J.* **159**, 102 (2020).

49. Murray, C. D. & Harper, D. Expansion of the planetary disturbing function to eighth order in the individual orbital elements. *QMW Maths Notes, No.15*, vii+436 (1993).

50. de Pater, I., Renner, S., Showalter, M.R.S. & Sicardy, B. in *Planetary ring systems* (eds Tiscareno, M. S. & Murray, C.D.) 112-124 (Cambridge Univ. Press, 2018).

51. Hamilton, D.P & Krivov, A.V. Circumplanetary dust dynamics: Effects of solar gravity, radiation pressure, planetary oblateness, and electromagnetism. *Icarus* **123**, 503–523. (1996)

52. Chambers, J. E. A Hybrid symplectic integrator that permits close encounters between massive bodies. *Mon. Not. R. Astr. Soc.* **304**, 793–799. (1999)

Competing interests
The authors declare no competing interests.

Inclusion & Ethics
This research includes data from observers

Author information
Correspondence and requests for materials should be addressed to B.E.M. at bmorgado@ov.ufrj.br.

Data availability
The observational data that support this paper and other findings of this study are available at CDS. For the purpose of open access, the authors have applied a creative commons attribution (CC BY) licence to any author accepted manuscript version arising.

Code availability
This research made use of SORA, a python package for stellar occultations reduction and analysis, developed with the support of ERC Lucky Star and LIneA/Brazil, within the collaboration Rio-Paris-Granada teams. Instructions for downloading and installing SORA can be found on PyPI (https://pypi.org/project/sora-astro/), on GitHub (https://github.com/riogroup/SORA) and on its online documentation (https://sora.readthedocs.io/).

The method and examples of earlier numerical simulations results have been summarised in ref[29], anybody interested in using this code in collaborative mode can contact HS.

Other specific codes written especially for this project are available from the corresponding author upon request.

Extended Data legends

Extended Data Table 1 | Parameters of the occulted stars, with their 1-σ error bars. [a] The time of closest geocentric approach of Quaoar's shadow. [b] The ICRS J2000 star coordinates and their uncertainties are propagated to the occultation epoch with SORA[36]. [c] To be compared with Quaoar's V magnitude, ∼18.9.

Extended Data Table 2 | Local ring parameters, with their 1-σ error bars. [a] Assuming a monolayer ring. [b] Assuming a polylayer ring. [c] The light curve S/N does not allowed the detection of the ring. [d] These values are not available as the ring is unresolved, only the Equivalent Width (Radial Width × Normal opacity) can be computed. [e] Due the small number of points within each detections, the 1-sigma uncertainty has a large asymmetry.

Extended Data Figure 1 | Multi-band light curve observed by HiPERCAM on 05 June 2019. The flux observed in the g_s, r_s, i_s and z_s bands (black points) and the models (red line) vs. time relative to the observer's closest approach time (03:00:31.858 UTC). The blue shaded regions are enlarged in the side panels. Only one common model (the one obtained for i_s) is plotted as no statistically significant differences are observed between filters (Table 1). Note the increase of the light curve quality with wavelength.

Extended Data Table 3 | Detection limit of material on chords without a ring detection. [a] Limits determined for the regions without detection, after the main event.

Extended Data Figure 2 | Dynamical environment of Quaoar's ring. The inner ellipse is Quaoar's Roche limit, assuming particles with bulk densities of $\rho = 400$ kg m^{-3}, see Methods for details. The corotation radius corresponds to the synchronous orbit, where the orbital period of particles matches Quaoar's rotation period. The blue and green zones delimit the location of the 1/3 Quaoar spin-orbit resonance (SOR) and the 6/1 Weywot mean motion resonance (MMR), respectively (Table 1). The width of each zone represents the 1-sigma uncertainties on the resonance locations, dominated by the uncertainty on Quaoar's mass. The two outer black ellipses outline the two possible Quaoar ring solution of Table 1.

Extended Data Figure 3 | Examples of Quaoar's ring time evolution. The run shown here uses an optical depth $\tau = 0.25$ and the Model 4 for the $\epsilon(v_n)$-relation (Extended Data Fig. 4). The curves show the evolution of radial velocity dispersion, labeled according to the bulk density ρ of the particles in kg m^{-3}. The thick black curves indicate that the system has formed a gravitational aggregate. The inserts (160 m × 160 m in size) show snapshots from the $\rho = 6,000$ kg m^{-3} case around the time when accretion begins. The labels indicate the time in units of orbital periods and the impact frequency f in units of impacts/particle/orbital period. Our criterion for detecting accretion is that f is larger than twice the average pre-accretion value of f, which corresponds to 189 orbital periods. For small ρ the steady state c_{st} is practically the same as in the non-gravitating case. The drop of c_{st} with larger ρ's follows from the pairwise pre-impact acceleration: increased impact speeds reduce the effective ϵ and thus allow for a lower c_{st} (ref.[43]).

Extended Data Figure 4 | Various models for the collisional restitution coefficient. Left: Model 1: Frost-covered ice spheres at temperature $T = 210$ K, $\epsilon(v_n) = (v_n/v_c)^{-0.234}$, with $v_c = 0.0077$ cm s^{-1} (ref.[25]); Model 2: Frost-covered ice at $T = 123$ K, $\epsilon(v_n) = 0.48{v_n}^{-0.20}$ (ref.[8]); Model 3: as Model 1 but with $v_c = 0.077$ cm s^{-1} (ten times the value of Model 1); Model 4: particles of radius $R = 20$ cm with compacted frost at $T = 123$ K, $\epsilon(v_n) = 0.90\exp(-0.22v_n) + 0.01{v_n}^{-0.6}$ (ref.[8]). Right: Theoretical relation for the dependence of critical coefficient of restitution ϵ_{cr} on optical depth, required for the balance between dissipation and the viscous gain of energy due to local viscosity[44]. In case of velocity-dependent

elasticity, the system adjusts its impact velocities (via velocity dispersion) so that the effective mean ϵ corresponds to the $\epsilon_{\mathsf{cr}}(\tau)$. In case of constant $\epsilon < \epsilon_{\mathsf{cr}}$ the system flattens to a near-monolayer state with a minimum $c \approx 2$ to $3Rn \approx 0.01$ cm s^{-1} $R/1$ m (where n is the mean motion) determined by the non-local viscous gain associated with the finite size of the particles. If the constant $\epsilon > \epsilon_{\mathsf{cr}}$, no thermal balance is possible and the system disperses via exponentially increasing c.

Extended Data Figure 5 | The influence of optical depth and particle size. In the upper panel, we show Model 4 simulations with $\tau = 0.25$ and $\tau = 1.0$. In both series of simulations particle size is $R = 1$ m. The same conventions as in Fig. 3 are used, but now the scale for c is linear, not logarithmic. For larger τ the steady-state velocity dispersion is reduced, and thus the condition $c_{\mathsf{st}}/v_{\mathsf{esc}} \lesssim 2$ is achieved for smaller ρ. The bottom panel compares the three assumed particle radii (0.33 m, 1 m, and 3 m) on accretion, using a common optical depth of $\tau = 0.25$ and assuming the velocity-dependent elasticity law of Model 2. Since c_{st} is nearly independent of R, the critical density corresponding to $c_{\mathsf{st}}/v_{\mathsf{esc}} \sim 2$ scales roughly as $\rho_{\mathsf{cr}} \propto 1/R^2$ since $v_{\mathsf{esc}} \propto \sqrt{R}$ (eq. (9)). Note that if a constant $\epsilon \lesssim 0.5$ is assumed, the particle size has no effect on the accretion limit, since in this case c_{st} scales linearly with R in a similar fashion to v_{esc}.

Extended Data Figure 6 | Topology of the Quaoar 1/3 Spin-Orbit Resonance (SOR). The bottom graph shows the maximum eccentricity e_{max} reached by a particle starting on an initially circular orbit of semi-major axis a perturbed by the Quaoar 1/3 SOR resonance. This resonance is driven by a mass anomaly whose amplitude is quantified by the dimensionless parameter $\epsilon_{1/3}$. The exact resonance radius $a_{1/3}$ is marked by the dashed vertical tick mark. The top plots show the phase portraits in the eccentricity vector space (X, Y) corresponding to particular values of a, with $X = e\cos(\phi_{1/3})$, $Y = e\sin(\phi_{1/3})$, where e is the orbital eccentricity and $\phi_{1/3} = (-\lambda' + 3\lambda - 2\varpi)/2$ is the resonant critical angle, see Methods for details. In an interval of width $W = (16|\epsilon_{1/3}|/3)a_{1/3}$ in semi-major axis centerd on the resonance, the origin of the phase portrait is an unstable hyperbolic point. Particles are then forced to reach a maximum eccentricity $e_{\mathsf{max}} = \sqrt{4/3}\sqrt{(W/2 - \Delta a)/a_{1/3}}$, where $\Delta a = a - a_{1/3}$ is the initial distance of the particle to the resonance. The value of e_{max} peaks at $e_{\mathsf{peak,1/3}} = (8/3)\sqrt{|\epsilon_{1/3}|/3}$ for $\Delta a = -(8/9)|\epsilon_{1/3}|a_{1/3}$. Outside this interval, $e_{\mathsf{max}} = 0$. Units are arbitrary in all the plots.

Extended Data Table 4 | Coefficients ϵ_k (Eq. 10 and refs[49, 48]) associated with the Quaoar 1/3 Spin Orbit Resonance (SOR) and the Weywot 6/1 Mean motion Resonances (MMRs). Note: depending on the line, λ' denotes either the orientation of Quaoar's mass anomaly or Weywot's mean longitude. The corotation term $\epsilon_{6/1,0}$ accounts for both the direct and indirect parts of Weywot's disturbing potential. See the Methods for the definition of the quantities.

Supplementary Information

Supplementary Table 1 - Circumstances of observations.

Site Ring status[a]	Longitude Latitude Altitude	Observers	Telescope aperture Detector Filter	Exposure time Cycle time (s)	Light curve RMS (flux)
		02 September 2018			
Les Makes	55^o 24' 36.3" E	S. Perrigault	60 cm	0.040	0.304
La Réunion	21^o 11' 56.1" S	J. P. Teng	Watec 910HX	0.040	
Unprobed – Negative	990 m		Clear		
HESS – Khomas	16^o 30' 06.9" E	F. Jankowsky	75 cm	0.095	0.052
Namibia	23^o 16' 16.6" S		DU888BV	0.095	
Positive – Unprobed	1800 m		Clear		
Upington	21^o 01' 31.6" E	M. Kretlow	25.4 cm	0.500	0.056
South Africa	28^o 03' 35.2" S		Raptor EM247	0.500	
Unprobed – Unprobed	870 m		Clear		
		05 June 2019			
PIRATE Mark III	16^o 30' 36.7" W	R. Busuttil	42.5 cm	8.00	0.231
Tenerife	28^o 17' 57.3" N	U. Kolb	FLI Proline	11.66	
Negative – Negative	2390 m	C. Snodgrass	Clear		
Artemis	16^o 30' 38.0" W	D. Sebastian	100 cm	2.50	0.039
Tenerife	28^o 18' 04.0" N	A. Burdanov	Andor Ikon	3.78	
Negative – Negative	2390 m	J. de Wit	Clear		
GTC	17^o 53' 30.2" W	V. S. Dhillon	1040 cm	0.130	0.117 – 0.036[(c)]
La Palma	28^o 45' 21.6" N	T. R. Marsh	HiPERCAM	0.135	
Positive – Positive	2270 m		$g_s r_s i_s z_s$[(b)]		
Liverpool	17^o 52' 45.1" W	P. Santos-Sanz	200 cm	0.60	0.221
La Palma	28^o 45' 44.5" N	J. L. Ortiz	EEV ANDOR	0.63	
Negative – Negative	2320 m	N. Morales	IR720		
TRAPPIST-North	07^o 51' 57.0" W	E. Jehin	60 cm	5.00	0.116
Morocco	31^o 12' 22.0" N	Z. Benkhaldoun	Andor IKONL	5.99	
Negative – Negative	2720 m		Clear		

[a] The first status is for the detection before closest approach and the seconds is for after it. Unprobed, means that the observation do not cover the region where the ring is expected to be seen. We highlight that the negative detections should be evaluated together with the S/N and the temporal resolution.
[b] Central wavelengths are g_s: 0.48 μm, r_s: 0.62 μm, i_s: 0.76 μm, z_s: 0.91 μm.
[c] The RMS of the light curve's decreases with wavelength with the following values in each band of g_s: 0.117, r_s: 0.044, i_s: 0.037, z_s: 0.036.

Supplementary Table 1 [Cont.] - Circumstances of observations.

Site Ring status	Longitude Latitude Altitude	Observers	Telescope aperture Detector Filter	Exposure time Cycle time (s)	Light curve RMS (flux)
11 June 2020					
ESA CHEOPS	(d)	CHEOPS's team	32 cm	3.000	0.008
			Teledyne CCD	3.024	
Positive – Positive			Clear		
Mount Carbine	144^o 52' 29.4" E	J. Broughton	25 cm	0.160	0.147
Australia	16^o 27' 58.7" S		Night Eagle	0.160	
Unprobed – Positive	57 m		Clear		
27 August 2021					
Glenlee	150^o 30' 01.6" E	S. Kerr	30.4 cm	0.32	0.13
Australia	23^o 16' 10.1" S		Watec 910BD	0.32	
Unprobed – Unprobed	53 m		Clear		
Samford Valley	152^o 50' 53.2" E	J. Bradshaw	35.6 cm	0.25	0.11
Australia	27^o 22' 07.0" S		ASI ZWO174MM	0.25	
Positive – Negative	80 m		Clear		
Algester	153^o 02' 14.0" E	R. Langersek	28.0 cm	0.50	0.15
Australia	27^o 36' 46.0" S		ASI-174MM PRO	0.50	
Positive – Negative	46 m		Clear		
Reedy Creek	153^o 23' 52.9" E	J. Broughton	51 cm	0.25	0.18
Australia	28^o 06' 30.4" S		QHY174-GPS	0.25	
Positive – Negative	66 m		Clear		
Hawkesbury Heights	150^o 38' 27.9" E	D. Gault	30.0 cm	0.32	0.14
Australia	33^o 39' 51.9" S		Watec WT-910BD	0.32	
Unprobed – Negative	273 m		Clear		
Hazelbrook	150^o 27' 06.5" E	P. Nosworthy	28.0 cm	0.32	0.15
Australia	33^o 42' 26.6" S		Watec 910BD	0.32	
Unprobed – Negative	648 m		Clear		
Yass	148^o 58' 35.06" E	W. Hanna	50.8 cm	0.25	0.13
Australia	34^o 51' 50.89" S		QHY174M-GPS	0.25	
Negative – Negative	536 m		Clear		
Murrumbateman	148^o 59' 56.0" E	D. Herald	40.0 cm	0.16	0.17
Australia	34^o 57' 31.3" S		Watec 910BD	0.16	
Unprobed – Negative	596 m		Clear		

[d] See details about the CHEOPS space telescope observations in ref[31].

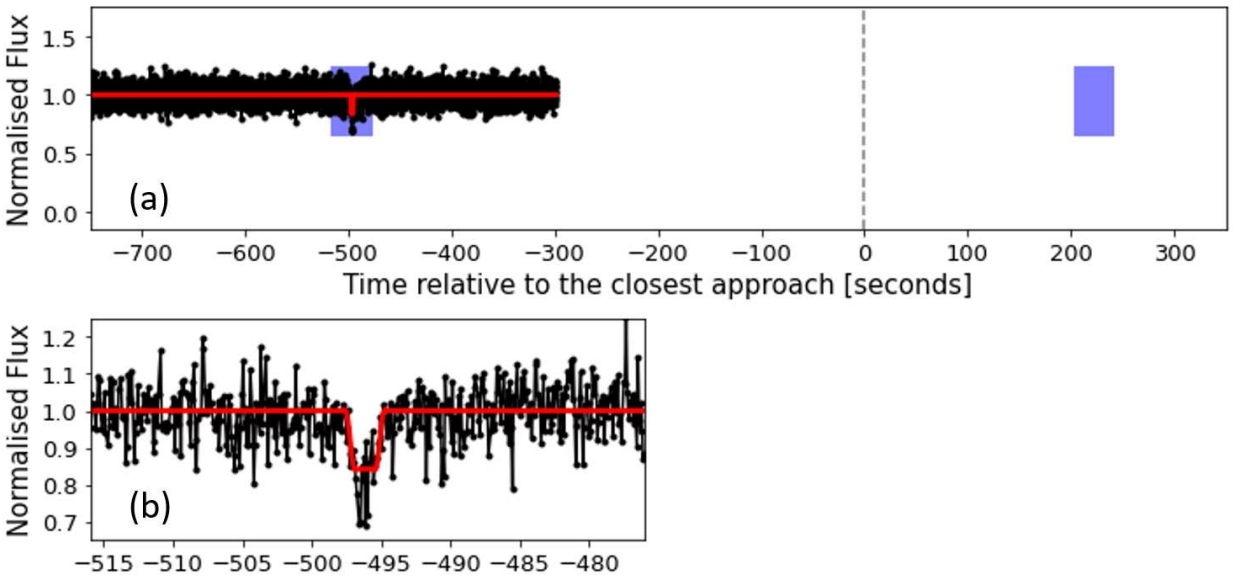

Supplementary Figure 1 | **The ring detection of 02 September 2018.** The observed flux (black points) and the model (red line) vs. time relative to the observer closest approach (18:16:10.895 UTC) at the HESS station on 02 September 2018. Panel a: general view of the light curve, note that no data were acquired after the closest approach around the expected ring detection (blue shaded regions). Panel b: enlargement of the overlying blue shaded region.

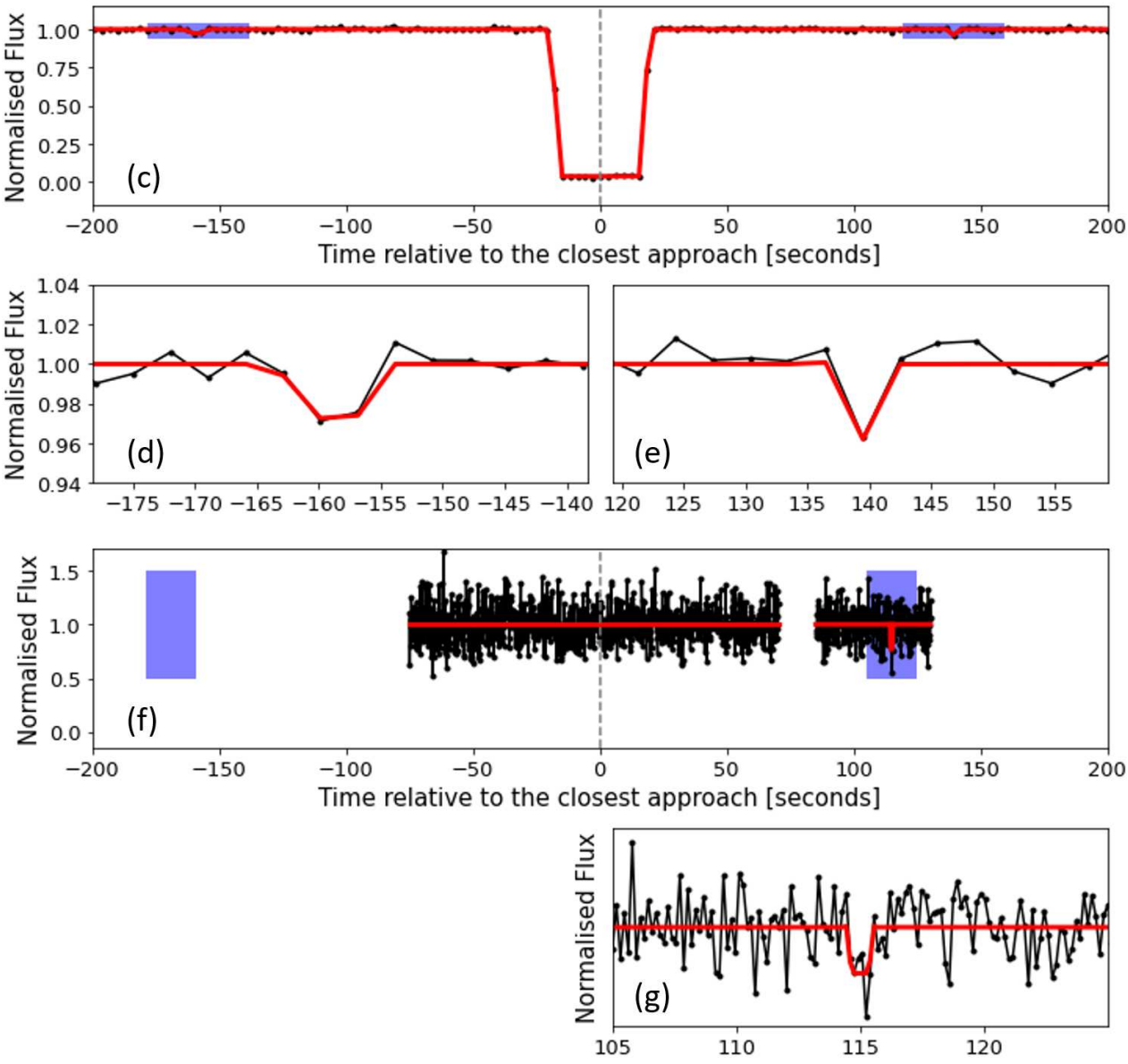

Supplementary Figure 1 [Cont.] | **Ring detections of 11 June 2020.** Panels c, d and e: the CHEOPS space telescope light curve (closest approach time at 16:27:25.662 UTC). Panels f and g: the light curve observed at Mount Carbine by J. Broughton (closest approach time at 16:30:51.615 UTC).

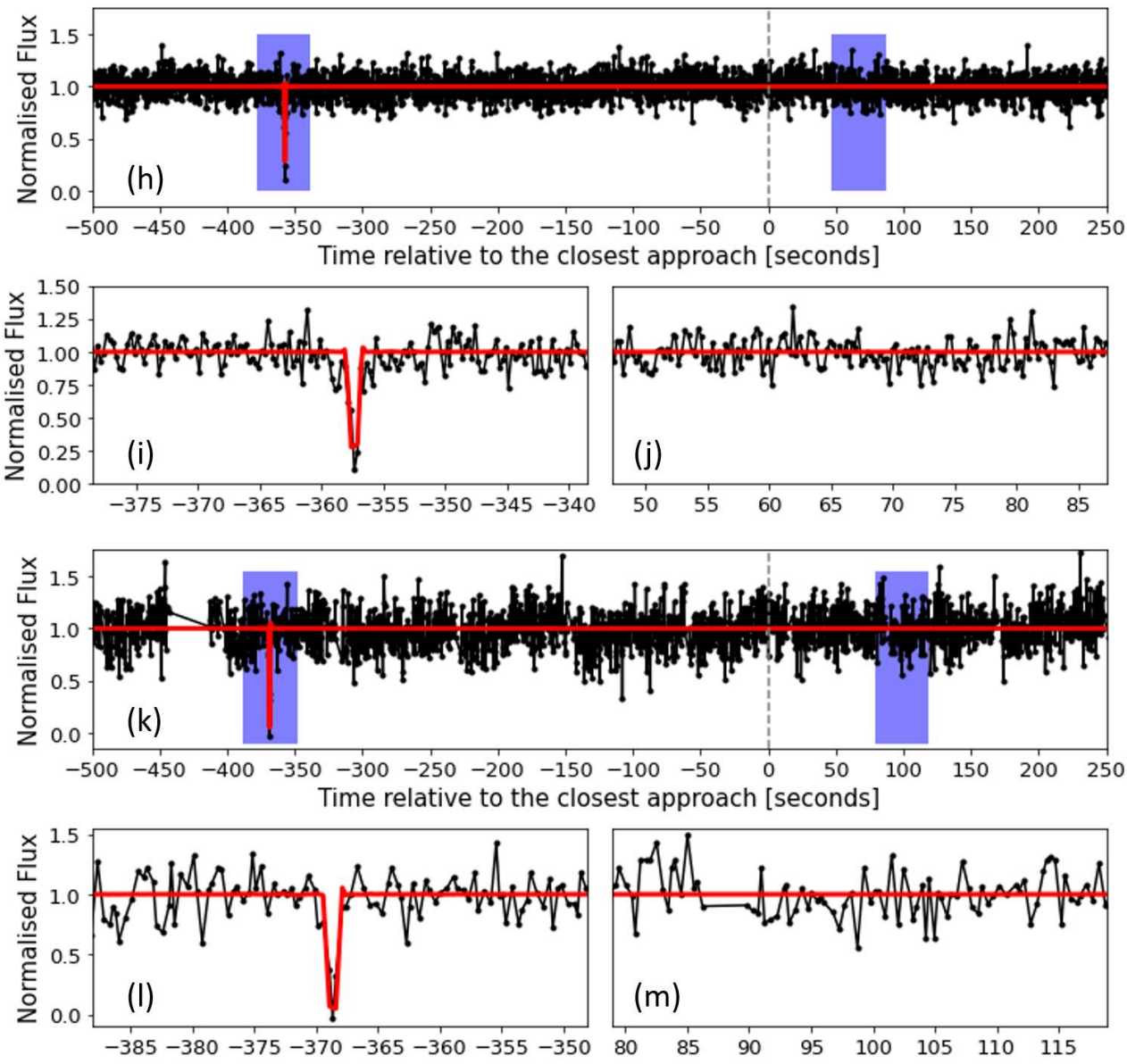

Supplementary Figure 1 [Cont.] | **The ring detection of 27 August 2021.** Panels h, i and j: the light curve observed in Samford Valley (closest approach time at 10:59:00.528 UTC). Panels k, l and m: the light curve observed in Reedy Creek (closest approach time at 10:59:00.096 UTC). Both light curve were obtained by citizen astronomers, the first by J. Bradshaw and the second by J. Broughton. A third, simultaneous detection is displayed in Fig. 1, panels d, e and f.

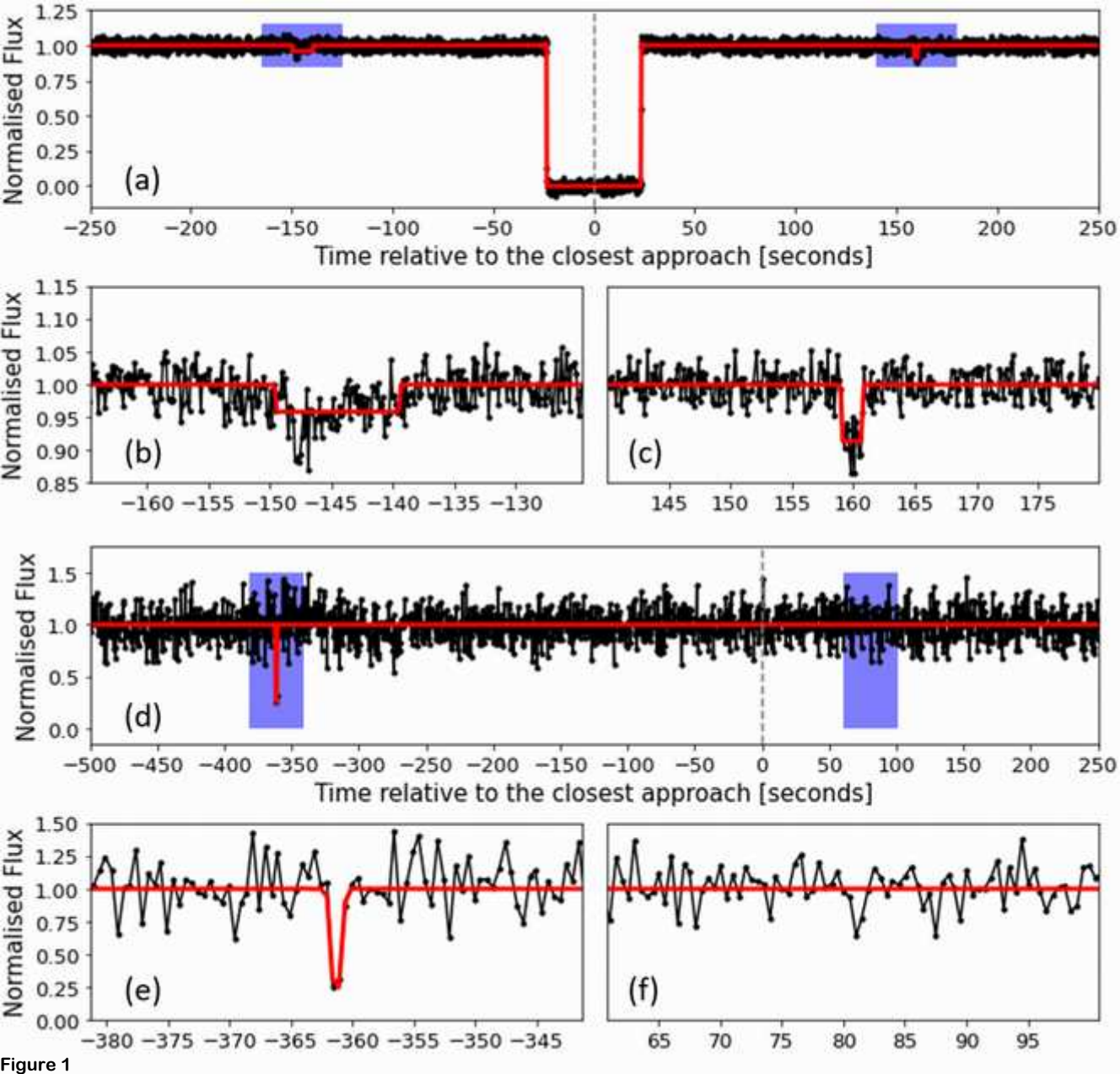
Normalised Flux
(a)
Time relative to the closest approach [seconds]
(b)
(c)
(d)
Time relative to the closest approach [seconds]
(e)
(f)

Figure 1

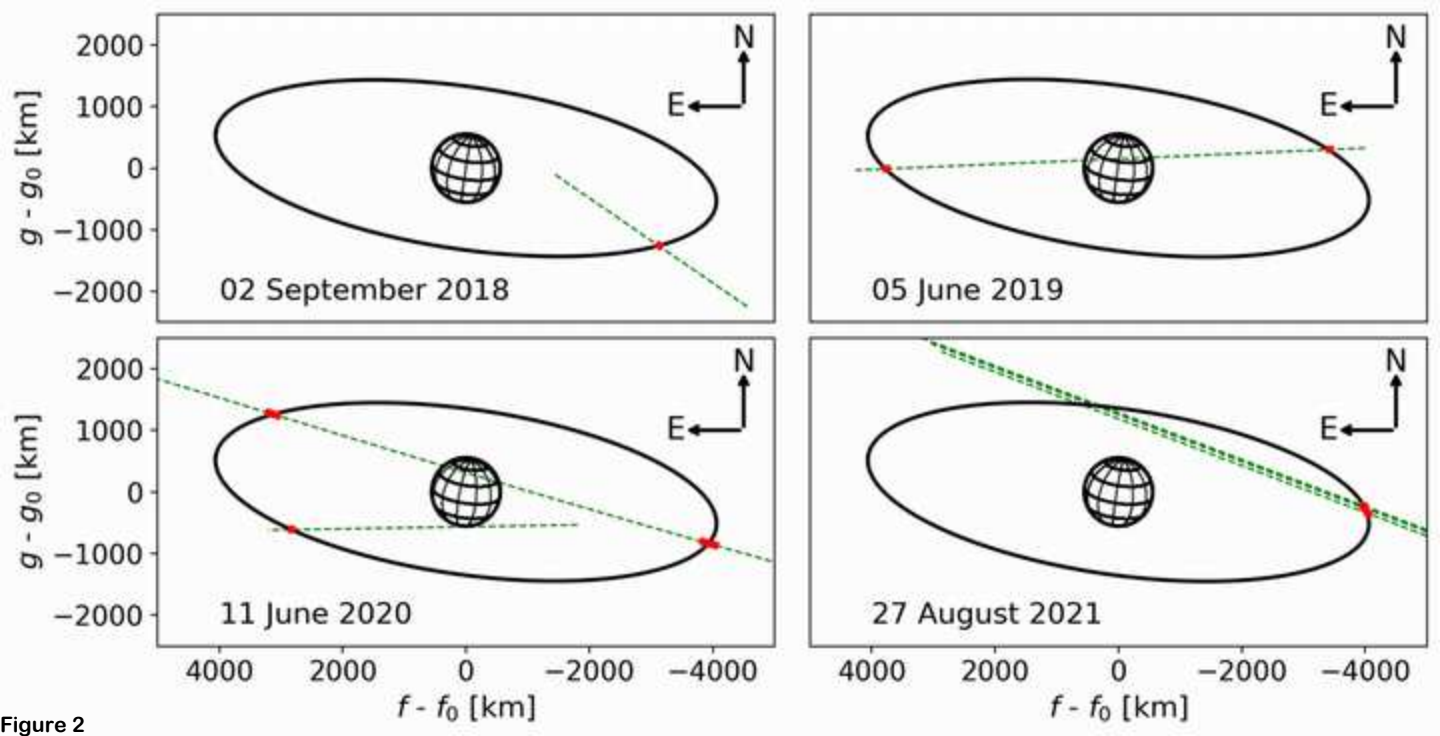
2000
1000
0
−1000
−2000
g - g0 [km]
N
E
02 September 2018
05 June 2019
11 June 2020
27 August 2021
4000
2000
0
−2000
−4000
f - f0 [km]

Figure 2

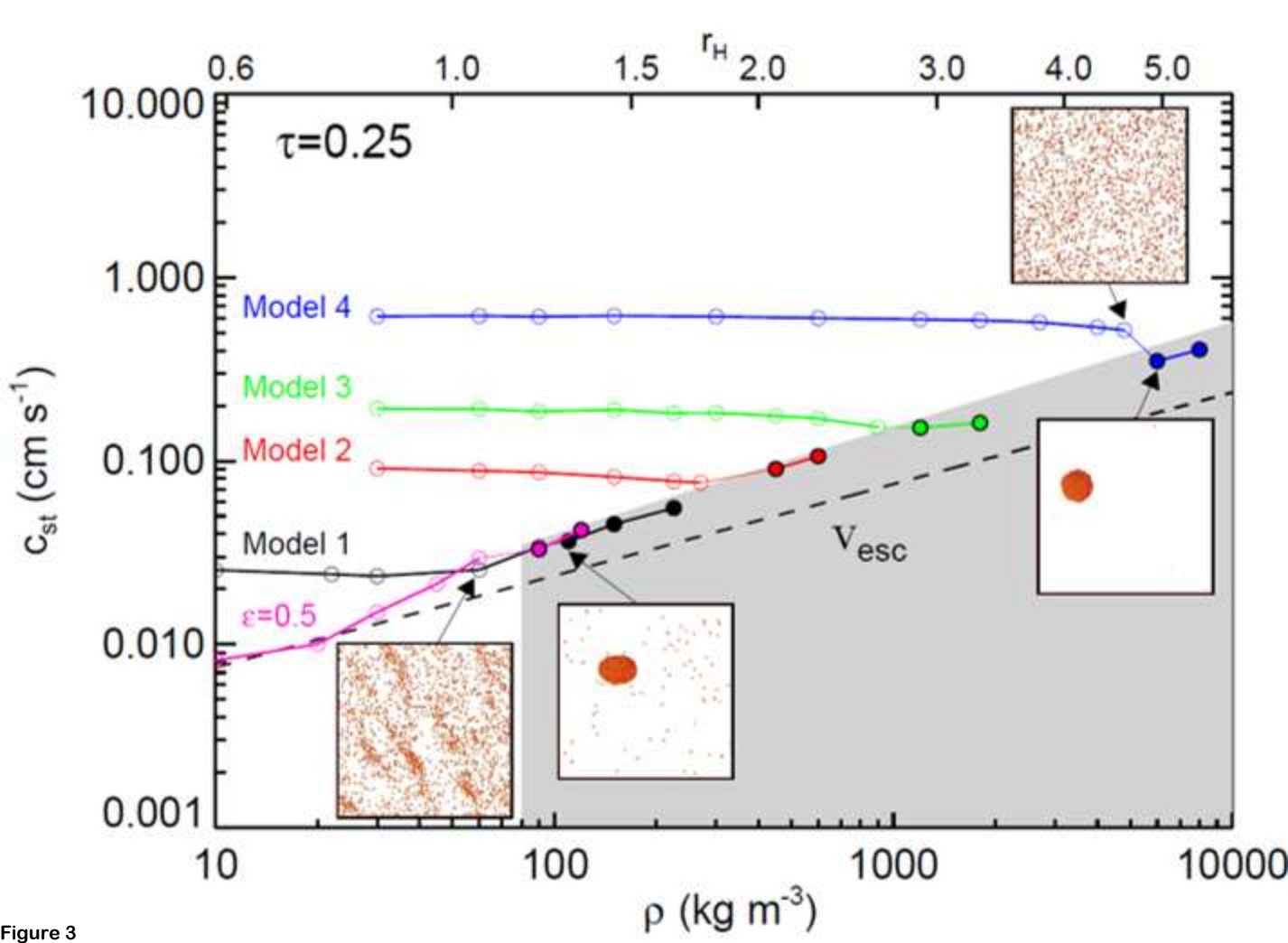
r_H
0.6
1.0
1.5
2.0
3.0
4.0
5.0
τ=0.25
Model 4
Model 3
Model 2
Model 1
ε=0.5
V_esc
c_st (cm s^-1)
10.000
1.000
0.100
0.010
0.001
10
100
1000
10000
ρ (kg m^-3)

Figure 3

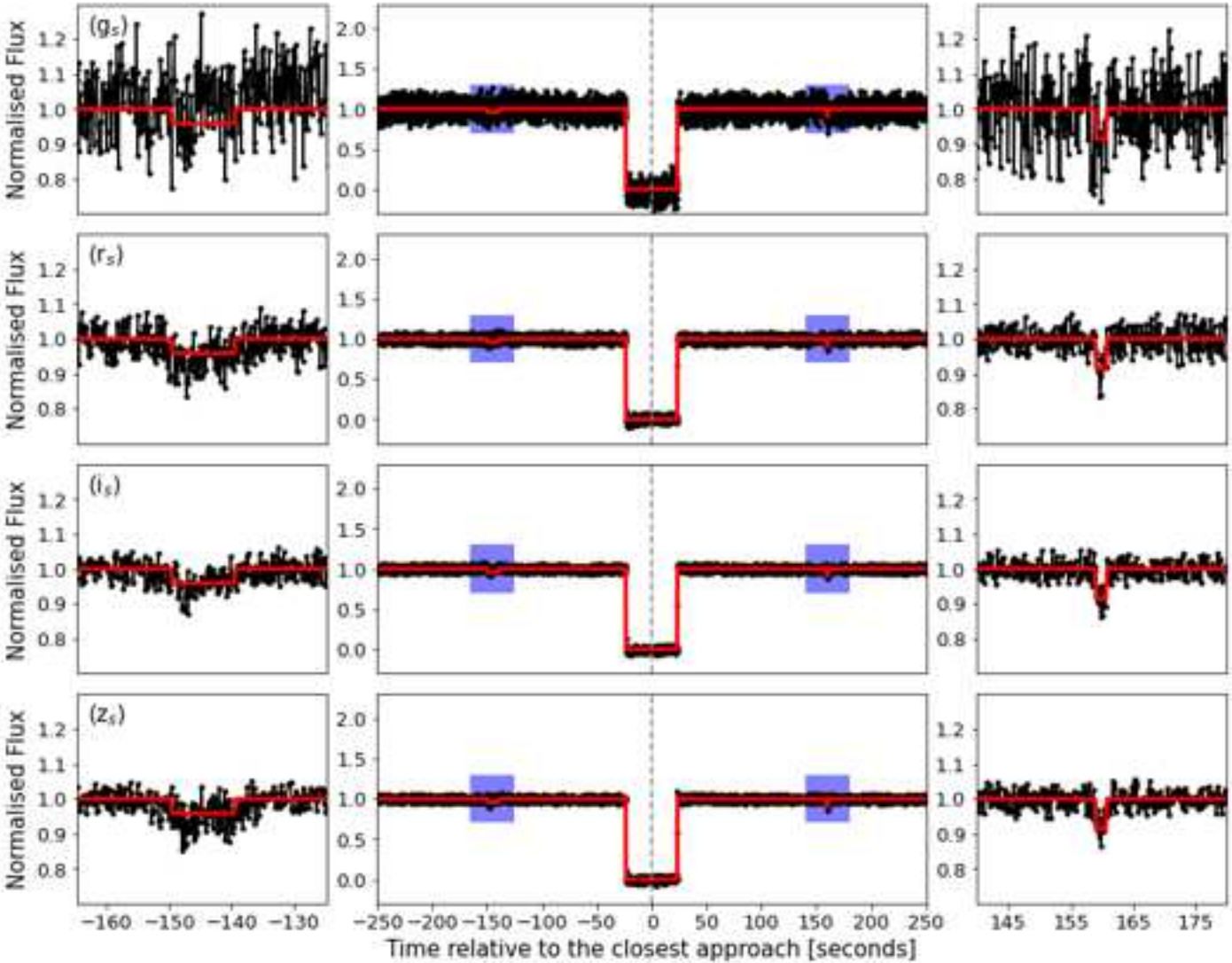

Extended Data Figure 1

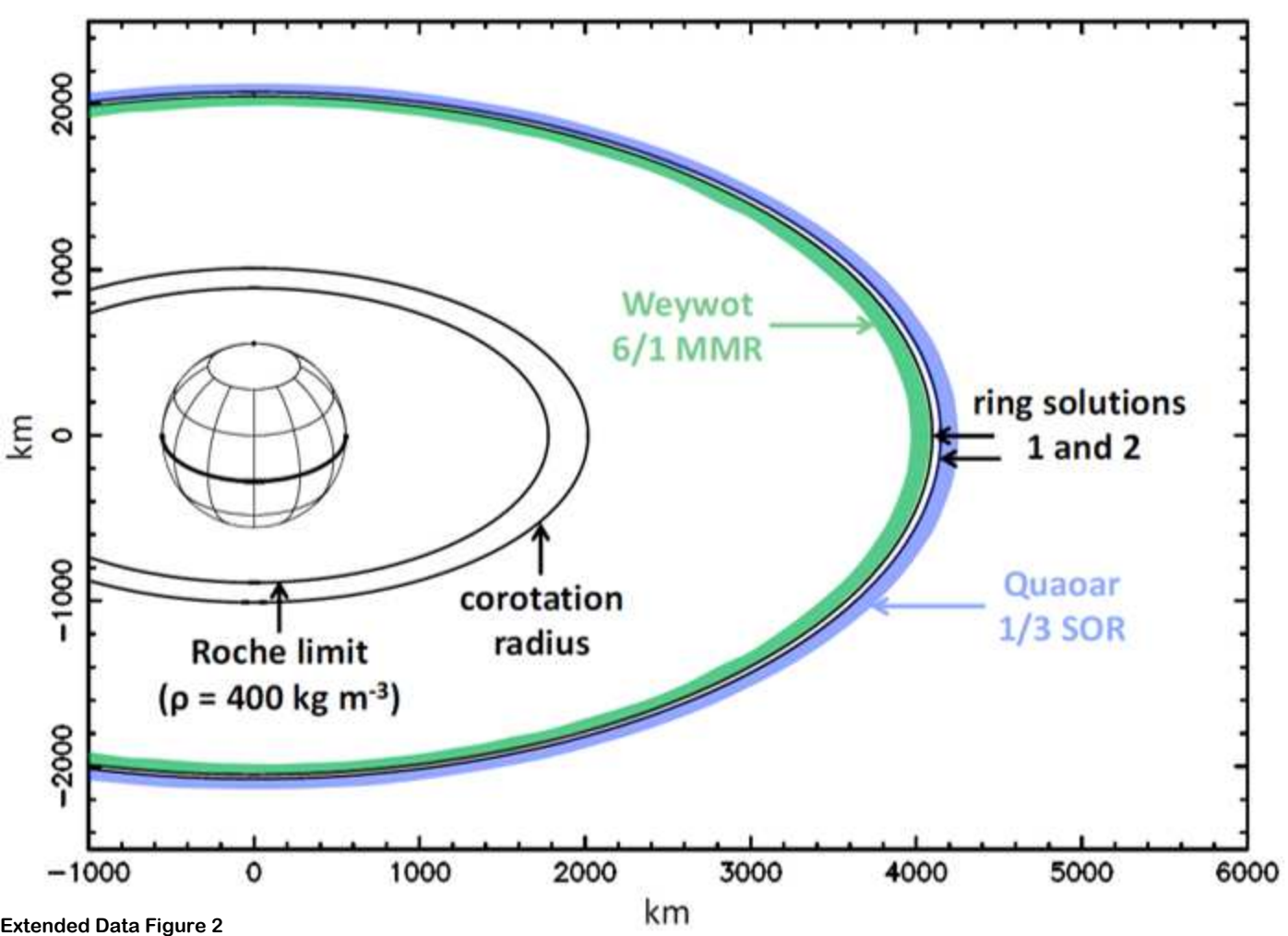

Extended Data Figure 2

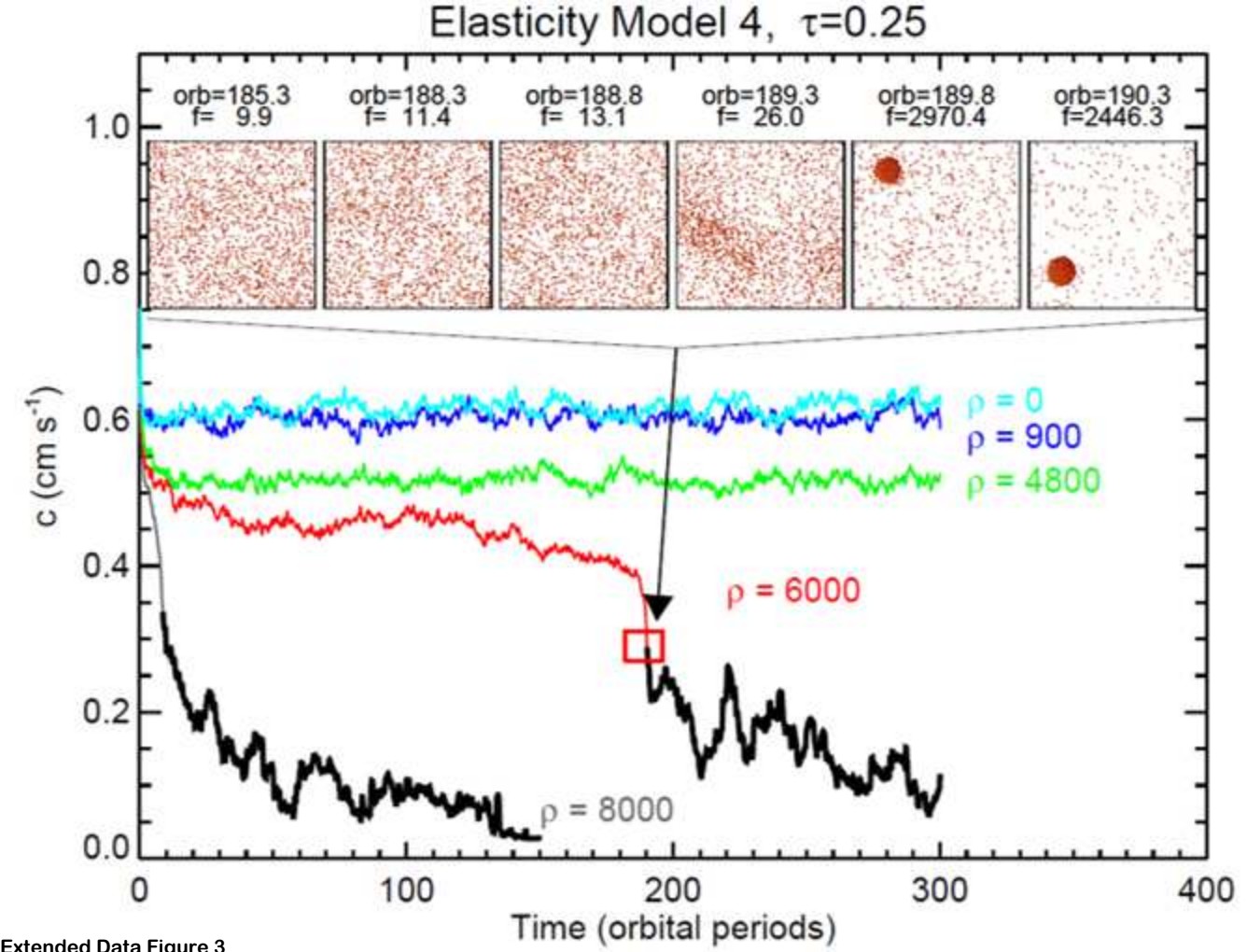

Extended Data Figure 3

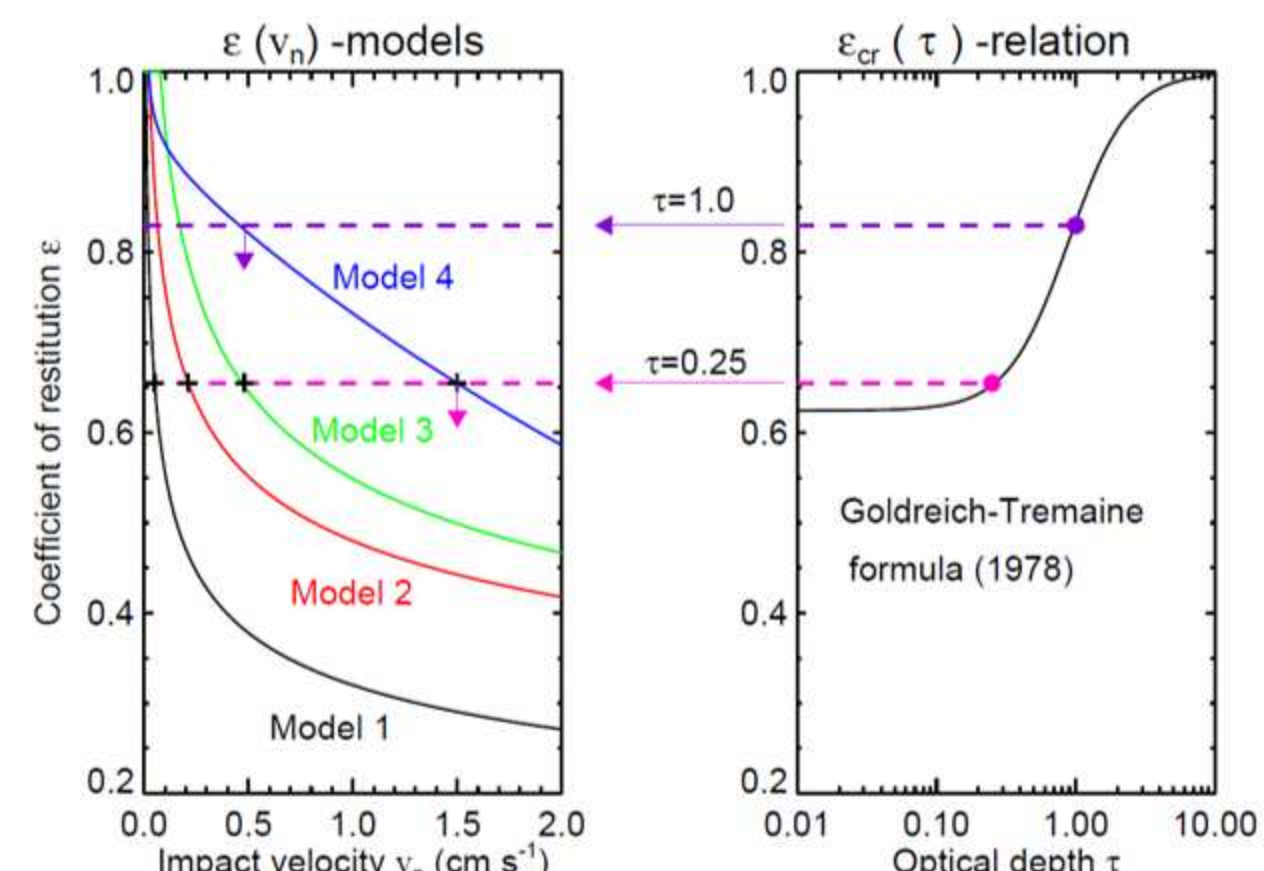

Extended Data Figure 4

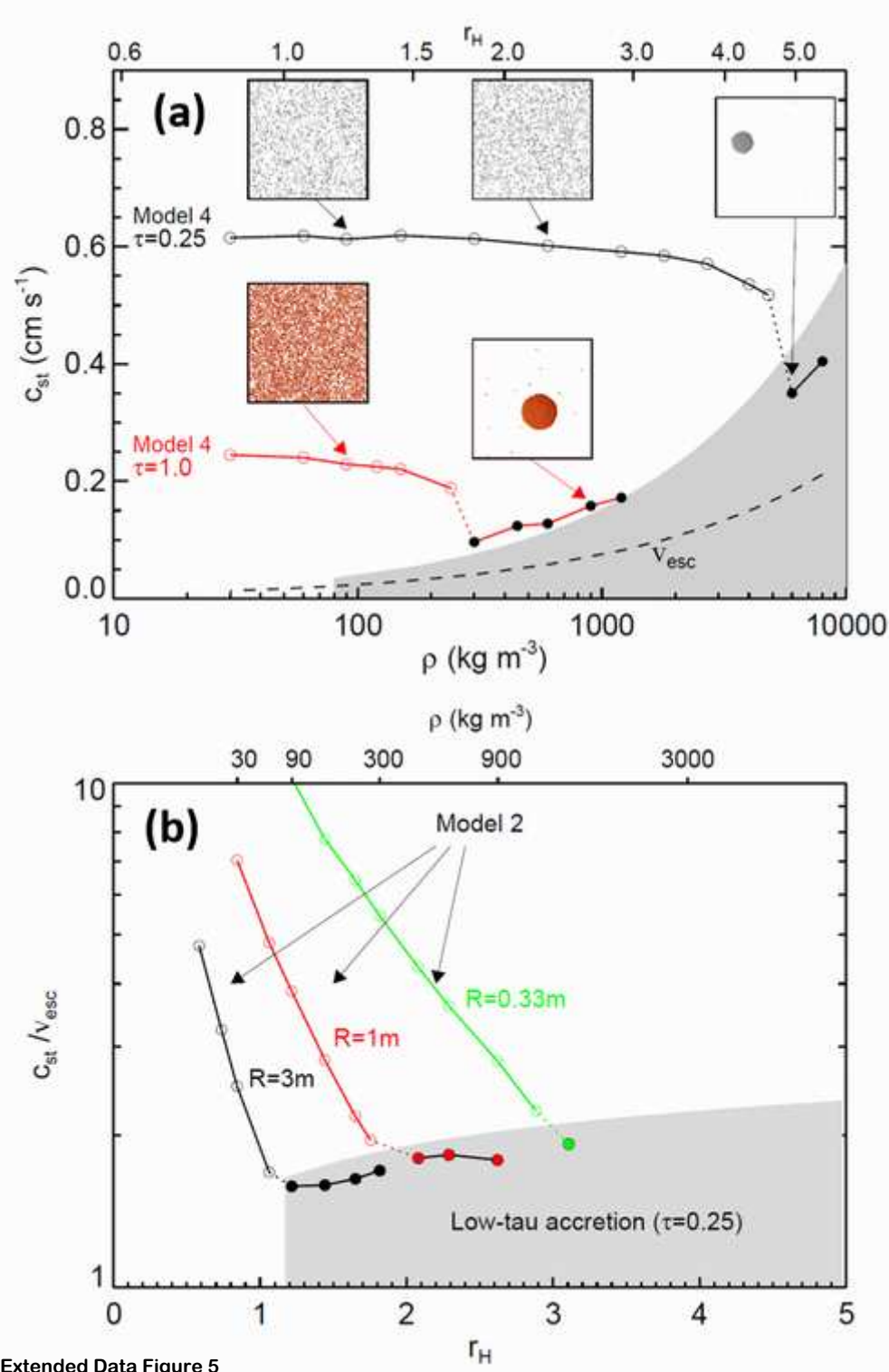

Extended Data Figure 5

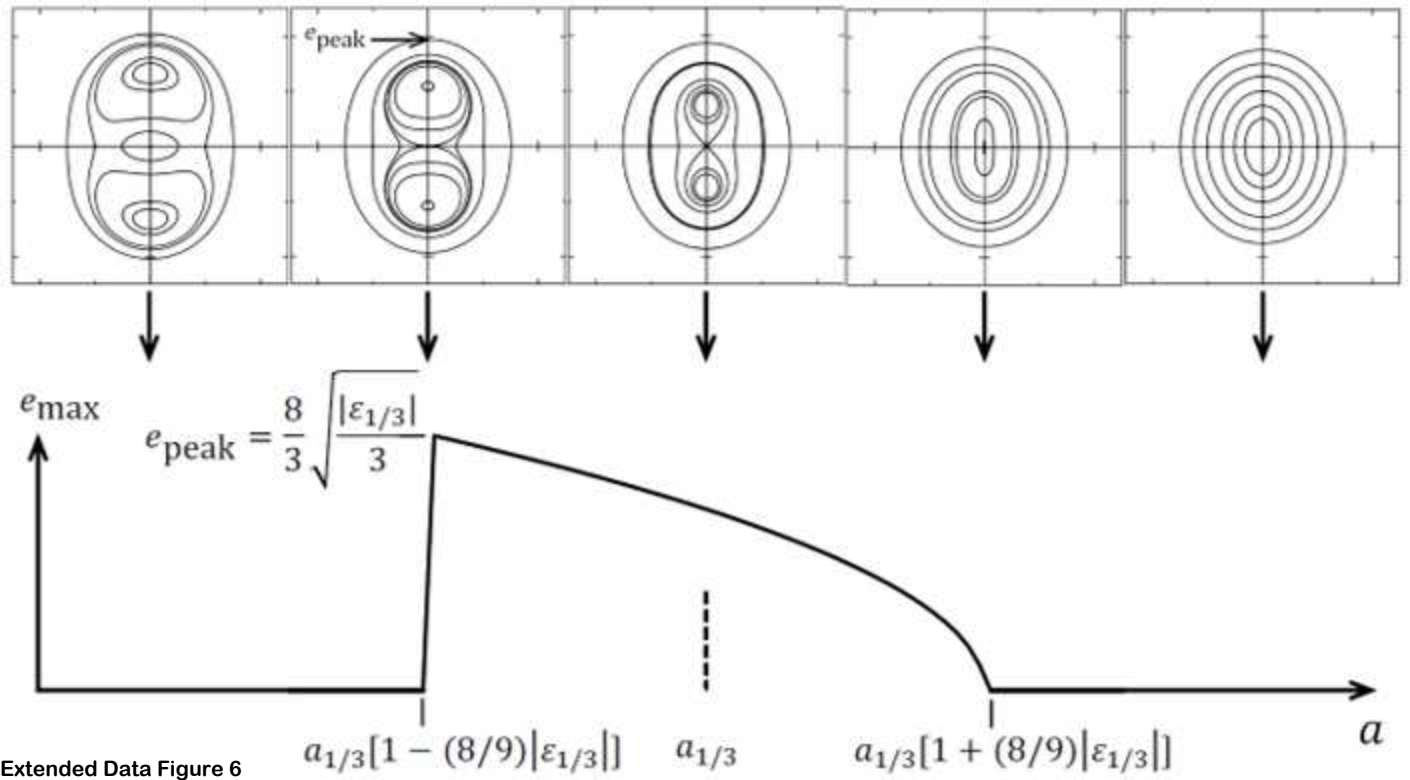

Extended Data Figure 6

Date and time UTC[a] dd-mm-yyyy hh:mm:ss	Gaia EDR3 source identifier	Right Ascension[b] hh mm ss.sss (mas)	Declination[b] dd mm ss.sss (mas)	G mag[c]
02-09-2018 18:16:56.90	4145444851530756224	17^h 59^m $02^s.05886$ (1.6)	-15° 28' 30".2066 (1.1)	12.7
05-06-2019 03:00:57.12	4146058516454329344	18^h 10^m $07^s.31110$ (0.5)	-15° 18' 12".3535 (0.3)	17.4
11-06-2020 16:27:25.50	4146202445050212352	18^h 15^m $03^s.05579$ (0.1)	-15° 15' 04".9460 (0.1)	12.7
27-08-2021 11:00:53.98	4146198047004695040	18^h 15^m $26^s.71666$ (0.3)	-15° 19' 21".0846 (0.2)	14.3

Extended Data Table 1

Date [dd-mm-yyyy]	Station	B [°]	r [km]	W_r [km]	p^f	r^f	$p^{\perp}$	$r^{\perp}$	E_p [km]	A_r [km]
02-09-2018	HESS (bef.)	−20.12	4,097.8 (0.6)	22.29 (1.27)	0.089 (0.007)	0.094 (0.008)	0.016 (0.001)	0.016 (0.001)	0.34 (0.03)	0.35 (0.03)
05-06-2019	GTC g_s (bef.)	−20.45	n.a.[c]	n.a.[c]	n.a.[c]	n.a.[c]	n.a.[c]	n.a.[c]	n.a.[c]	n.a.[c]
05-06-2019	GTC r_s (bef.)	−20.45	4,114.5 (12.3)	336.34 (23.81)	0.027 (0.006)	0.027 (0.006)	0.005 (0.003)	0.005 (0.002)	1.70 (0.41)	1.71 (0.41)
05-06-2019	GTC i_s (bef.)	−20.45	4,126.4 (1.1)	301.38 (2.50)	0.020 (0.001)	0.020 (0.001)	0.003 (0.001)	0.004 (0.001)	1.04 (0.07)	1.04 (0.07)
05-06-2019	GTC z_s (bef.)	−20.45	4,124.8 (1.2)	306.55 (2.36)	0.026 (0.002)	0.026 (0.002)	0.004 (0.001)	0.004 (0.001)	1.39 (0.10)	1.41 (0.11)
05-06-2019	GTC g_s (aft.)	−20.45	4,047.5 (31.0)	109.68 (61.45)	0.048 (0.013)	0.050 (0.014)	0.009 (0.002)	0.009 (0.003)	0.87 (0.55)	0.88 (0.56)
05-06-2019	GTC r_s (aft.)	−20.45	4,077.9 (2.4)	40.69 (4.83)	0.050 (0.006)	0.052 (0.006)	0.009 (0.001)	0.009 (0.001)	0.35 (0.04)	0.35 (0.04)
05-06-2019	GTC i_s (aft.)	−20.45	4,078.4 (0.5)	44.09 (1.05)	0.045 (0.003)	0.046 (0.003)	0.008 (0.001)	0.008 (0.001)	0.35 (0.02)	0.36 (0.02)
05-06-2019	GTC z_s (aft.)	−20.45	4,042.3 (31.3)	109.78 (63.00)	0.037 (0.010)	0.038 (0.010)	0.007 (0.002)	0.007 (0.002)	0.75 (0.45)	0.76 (0.46)
11-06-2020	CHEOPS (bef.)	−20.51	4,114.0 (12.4)	n.a.[d]	n.a.[d]	n.a.[d]	n.a.[d]	n.a.[d]	0.72 (0.37)	n.a.[d]
11-06-2020	CHEOPS (aft.)	−20.51	4,127.6 (36.8)	n.a.[d]	n.a.[d]	n.a.[d]	n.a.[d]	n.a.[d]	0.67 (0.48)	n.a.[d]
11-06-2020	Mt. Carbine (aft.)	−20.51	4,029.5 (1.5)	21.34 (3.13)	0.137 (0.038)	0.148 (0.045)	0.025 (0.007)	0.026 (0.008)	0.53 (0.15)	0.55 (0.16)
27-08-2021	Reedy Creek (bef.)[e]	−20.48	4,112.7 (1.2)	$4.91^{+6.94}_{-3.43}$	$0.988^{+0.012}_{-0.006}$	$4.425^{+3.622}_{-3.604}$	$0.312^{+0.032}_{-0.204}$	$0.774^{+0.634}_{-0.645}$	$1.53^{+0.28}_{-0.81}$	$3.80^{+3.13}_{-3.47}$
27-08-2021	Algester (bef.)[e]	−20.48	4,095.3 (0.6)	$6.69^{+2.50}_{-1.02}$	$0.944^{+0.056}_{-0.053}$	$2.880^{+6.330}_{-2.262}$	$0.267^{+0.079}_{-0.174}$	$0.504^{+1.107}_{-0.206}$	$1.78^{+0.73}_{-0.99}$	$3.37^{+7.06}_{-2.43}$
27-08-2021	S. Valley (bef.)[e]	−20.48	4,092.7 (0.3)	$7.09^{+0.86}_{-0.52}$	$0.490^{+0.058}_{-0.070}$	$0.673^{+0.121}_{-0.129}$	$0.100^{+0.015}_{-0.017}$	$0.118^{+0.021}_{-0.023}$	$0.71^{+0.10}_{-0.10}$	$0.84^{+0.14}_{-0.14}$

Extended Data Table 2

Date	Site	Original spatial resolution		Resampled data		
		W_r [km]	$E_p(3\sigma)$ [km]	W_r [km]	$E_p(3\sigma)$ [km]	N
2018-09-02	Les Makes	0.261	0.040	299.799	0.004	1150
2019-06-05	PIRATE - Tenerife	189.005	22.663	378.010	22.663	2
2019-06-05	Artermis - Tenerife	59.064	1.188	295.321	0.862	5
2019-06-05	Liverpool - La Palma	14.175	2.110	297.677	0.744	21
2019-06-05	TRAPPIST-North	118.006	7.509	236.001	7.509	2
2021-08-27	Glenlee (AUS)	3.413	0.225	296.983	0.070	87
2021-08-27	Hawkesbury Heights (AUS)	3.402	0.230	299.374	0.071	88
2021-08-27	Hazelbrook (AUS)	3.402	0.258	299.368	0.069	88
2021-08-27	Yass (AUS)	2.658	0.166	297.707	0.050	112
2021-08-27	Murrumbateman (AUS)	1.701	0.152	299.402	0.027	176
2021-08-27	Reed Creek[a] (AUS)	2.662	0.233	298.125	0.040	112
2021-08-27	Algester[a] (AUS)	5.325	0.389	298.202	0.074	56
2021-08-27	Samford Valley[a](AUS)	2.663	0.140	298.212	0.030	112

Extended Data Table 3

1/3 Quaoar SOR				
Order k in e	$\epsilon_{1/3,2}$	Total order in e and e'	$\phi_{1/3}$	Name
2	$-0.005848\mu_{\mathrm{Q}}$	e^2	$(-\lambda' + 3\lambda - 2\varpi)/2$	1/3 SOR
6/1 Weywot MMRs				
	$\epsilon_{6/1,k}$	$e^k e'^{5-k}$	$\phi_{6/1,k}$	Name
0	$-0.1457\mu_{\mathrm{W}}$	e'^5	$6\lambda' - \lambda - 5\varpi'$	6/1 corotation
1	$+2.338\mu_{\mathrm{W}}$	ee'^4	$6\lambda' - \lambda - \varpi - 4\varpi'$	6/1 Lindblad
2	$-1.705\mu_{\mathrm{W}}$	$e^2e'^3$	$(6\lambda' - \lambda - 2\varpi - 3\varpi')/2$	6/1 2nd-order
3	$+0.6158\mu_{\mathrm{W}}$	$e^3e'^2$	$(6\lambda' - \lambda - 3\varpi - 2\varpi')/3$	
4	$-0.1103\mu_{\mathrm{W}}$	e^4e'	$(6\lambda' - \lambda - 4\varpi - \varpi')/4$	
5	$+0.007852\mu_{\mathrm{W}}$	e^5	$(6\lambda' - \lambda - 5\varpi)/5$	

Extended Data Table 4